Pyramidal cell types drive functionally distinct cortical activity patterns during decision-making

Simon Musall[1,2,8], Xiaonan R. Sun[3,4,8], Hemanth Mohan[3,5], Xu An[3,5], Steven Gluf[3], Shujing Li[3], Rhonda Drewes[3], Emma Cravo[2], Irene Lenzi[1,2], Chaoqun Yin[6], Björn M. Kampa[2,7], Anne K. Churchland[3,6]

[1]Institute of Biological Information Processing (IBI-3), Forschungszentrum Jülich, Jülich, Germany

[2]Department of Neurophysiology, Institute for Zoology, RWTH Aachen University, Aachen, Germany

[3]Cold Spring Harbor Laboratory, Neuroscience, Cold Spring Harbor, NY, USA

[4]Department of Neurosurgery, Zucker School of Medicine, Hofstra University, Hempstead, NY, USA

[5]Department of Neurobiology, Duke University Medical Center, Durham, NC

[6]Department of Neurobiology, David Geffen School of Medicine, University of California, Los Angeles, CA, USA.

[7]JARA Brain, Institute for Neuroscience and Medicine, Forschungszentrum Jülich, Germany

[8]These authors contributed equally

Abstract

Understanding how cortical circuits generate complex behavior requires investigating the cell types that comprise them. Functional differences across pyramidal neuron (PyN) types have been observed within cortical areas, but it is not known whether these local differences extend throughout the cortex, nor whether additional differences emerge when larger-scale dynamics are considered. We used genetic and retrograde labeling to target pyramidal tract (PT), intratelencephalic (IT) and corticostriatal projection neurons and measured their cortex-wide activity. Each PyN type drove unique neural dynamics, both at the local and cortex-wide scale. Cortical activity and optogenetic inactivation during an auditory decision task also revealed distinct functional roles: all PyNs in parietal cortex were recruited during perception of the auditory stimulus, but, surprisingly, PT neurons had the largest causal role. In frontal cortex, all PyNs were required for accurate choices but showed distinct choice-tuning. Our results reveal that rich, cell-type-specific cortical dynamics shape perceptual decisions.

Introduction

The neocortex is organized into discrete layers that form a vertically-arranged microcircuit motif. This core circuit is largely conserved across cortical areas with each layer consisting of distinct excitatory and inhibitory cell types that can be categorized based on genetic markers, cell morphology, anatomical projections or developmental lineage[1]. The precise interplay between these cell types is crucial for accurate cortical circuit function and their respective functional roles are the subject of intense study. Tremendous progress has been made particularly for cortical interneurons, where the availability of specific mouse driver lines has revealed the functional arrangement of inhibitory circuit motifs[2–4], e.g. for network synchronization[5–7] and state-dependent sensory processing[8–11]. However, the roles of glutamatergic pyramidal neuron (PyN) types are less well established, although PyNs comprise ~80% of all cortical neurons and form almost all long-range projections that enable the communication between local cortical circuits and other brain areas.

While often treated as a monolithic group, PyNs appear to be far more diverse than interneurons with at least one hundred putative subtypes indicated by RNA sequencing[12]. These molecular signatures are critical for categorizing PyNs and go far beyond layer identity as different

subtypes are often intermingled within the same layers[13–17]. PyNs can also be classified based on their projection target. Long-range projection neurons are broadly categorized into two major types: intratelencephalic (IT) neurons, projecting to other cortical structures and the striatum, and pyramidal tract (PT) neurons, projecting to subcortical structures, such as the superior colliculus (SC), thalamus, the pons and the striatum. Furthermore, PT and IT neurons differ in their electrophysiological properties, dendritic morphology, local connectivity, and responsiveness to sensory stimulation[15–17]. Recent studies in sensory cortex also showed that only PT but not IT neurons are important for active perception of tactile or visual stimuli, suggesting that PT and IT neurons encode separate streams of information[18,19]. Similar results have been found in secondary motor cortex (M2), where specific PT neurons are involved in motor generation[13,20]. This suggests that the functional divergence of PyN types could be key for understanding cortical microcircuits, with PT and IT neurons forming functionally-distinct, parallel subnetworks that independently process different information. However, the functional tuning of individual PyNs in frontal cortex is still best predicted by cortical area location instead of laminar location or projection type[21]. Since PyN subtype activity has only been studied in single areas, it is therefore not known whether PyN-specific subcircuits exist throughout the cortex or only in a subset of cortical regions.

An ideal method to address this question is widefield calcium imaging, which allows measuring neural activity across the dorsal cortex with cell-type specificity[22–24]. Interneuron-specific widefield imaging revealed clear differences in the spatiotemporal dynamics of different inhibitory cell types during an odor detection task[25]. However, cortex-wide studies of different PyN types are lacking, in part due to the limited availability of PyN-specific driver lines[26–28]. Here, we used two novel knock-in mouse driver lines targeting PT or IT neurons[26] and performed widefield Ca^{2+} imaging to measure PyN subtype-specific activity while animals performed a perceptual decision-making task. Moreover, we developed a retrograde labeling approach to selectively measure the activity of corticostriatal projection (CStr) neurons throughout the dorsal cortex. Dimensionality-reduction and clustering analyses revealed unique cortex-wide dynamics for each PyN subtype, suggesting the existence of specialized subcircuits. Cortical dynamics of different PyNs were further segregated based on their role in decision-making, with encoder and decoder approaches revealing the strongest stimulus- and choice-related modulation in sensory, parietal and frontal cortices. This was confirmed by PyN-type-specific inactivation experiments. In parietal cortex, PT neurons were most important for sensory processing while all PyN types in frontal cortex were needed for choice formation and retention. Taken together, our results demonstrate that different PyN-types exhibit functionally distinct, cortex-wide neural dynamics with separate roles during perceptual decision-making.

Results

To monitor PyN-type specific neural activity throughout the dorsal cortex, we used two knock-in inducible CreER lines that target developmentally-distinct classes of excitatory cortical neurons: Fezf2-CreER targeting PT neurons and PlexinD1-CreER targeting IT neurons[26]. For PyN-type specific GCaMP6s expression, both lines were crossed with the Ai162 reporter line[29] and CreER activity was induced at four weeks of age. In each mouse line, GCaMP expression was restricted to specific cortical layers and PyN types (Fig 1a,b). In Fezf2 mice, expression was concentrated in layer 5b (Fig. 1a). We observed axonal projections to multiple subcortical regions, such as striatum and the corticospinal tract, confirming that Fezf2 is a reliable marker for corticofugal PT neurons. In PlexinD1 mice, GCaMP expression was restricted to layer 2/3 and layer 5a and axonal projections were visible in the corpus callosum and the striatum (Fig. 1b). These results

are in agreement with earlier reports[26], confirming that PlexinD1 is a reliable marker for intracortical and corticostriatal IT neurons.

After confirming non-overlapping expression patterns of PT and IT neurons, we measured cell-type-specific cortical activity with widefield calcium imaging. All imaging data was aligned to the Allen Common Coordinate Framework v3 (CCF)[25,30] to compare activity across individuals and PyN types. Both lines yielded robust GCaMP-dependent fluorescence and we observed rich neural dynamics throughout the dorsal cortex (Supp. Movies 1-3). We first used retinotopic mapping to assess sensory responses of different PyN types and the resulting spatial arrangement of visual areas. Both PT and IT neurons robustly responded to visual stimulation and we could construct retinotopic maps that reliably indicated the location of known visual areas (Fig. 1c)[31]. Retinotopic maps were similar to those observed in an Ai93D;Emx-Cre;LSL-tTA mouse line (EMX) that expressed GCaMP6f in all excitatory cortical neurons[32], suggesting that the functional architecture of visual areas is comparable across PyN types. However, clear differences were apparent in the modulation of cortical regions in the absence of visual stimulation (Fig. 1d, same individual mice as in 1c). For example, the total variance of cortex-wide activity was largest in parietal and frontal regions in PT neurons (Fig. 1d, left) while variance was highest in visual and somatosensory regions of IT neurons (Fig. 1d, center). This was comparable to variance in EMX mice, which showed additional modulation in retrosplenial (RS) cortex (Fig. 1d, right). These different patterns were also highly consistent across individual mice of the same PyN type (Supp. Fig. 1).

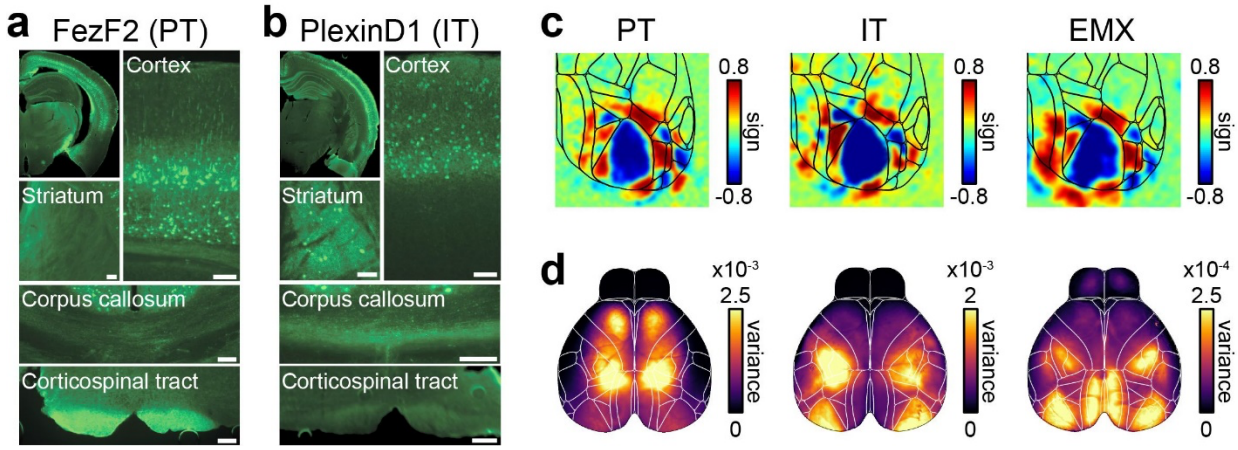

Figure 1. Knock-in mouse lines enable PyN subtype-specific recordings of cortex-wide neural activity. **a)** GCaMP6s expression in Fezf2-CreER;Ai162 mice. Cortical labeling is largely confined to layer 5b. Axonal projections were found in multiple subcortical regions such as the striatum and the corticospinal tract. (Scale bars: 100 µm). **b)** GCaMP6s expression in PlexinD1-CreER; Ai162 mice is widespread throughout the cortex and restricted to superficial layers 2/3 and layer 5a. Axonal projections were found in striatum and corpus callosum but absent in the corticospinal tract. **c)** Visual sign maps from retinotopic mapping experiments. IT and PT populations showed clear retinotopic responses in primary and secondary visual areas where boundaries largely resembled known areas that were also observed in nonspecific PyNs (EMX mice). **d)** Total variance maps from same mice as in c), showing most modulated cortical regions in each PyN type.

The observed differences in variance could indicate general differences in the spatiotemporal dynamics of cortex-wide activity across PyN types. To describe such differences, we performed semi-nonnegative matrix factorization (sNMF), reducing the imaging data to a small number of spatial- and temporal components that capture nearly all variance (>99%)[23,33]. Here, dimensionality (the number of required components) is a measure of the overall complexity of cortical dynamics. Surprisingly, PT neurons had much lower dimensionality compared to IT neurons (Fig. 2a), suggesting that PT neurons are more functionally-homogeneous. This was also

seen in the correlations between cortical regions, which were consistently highest for PT neurons (Supp. Fig. 2). A potential reason for this difference could be that IT neurons encompass a larger number of specialized subtypes than PT neurons and may thus support a wider range of functions[34].

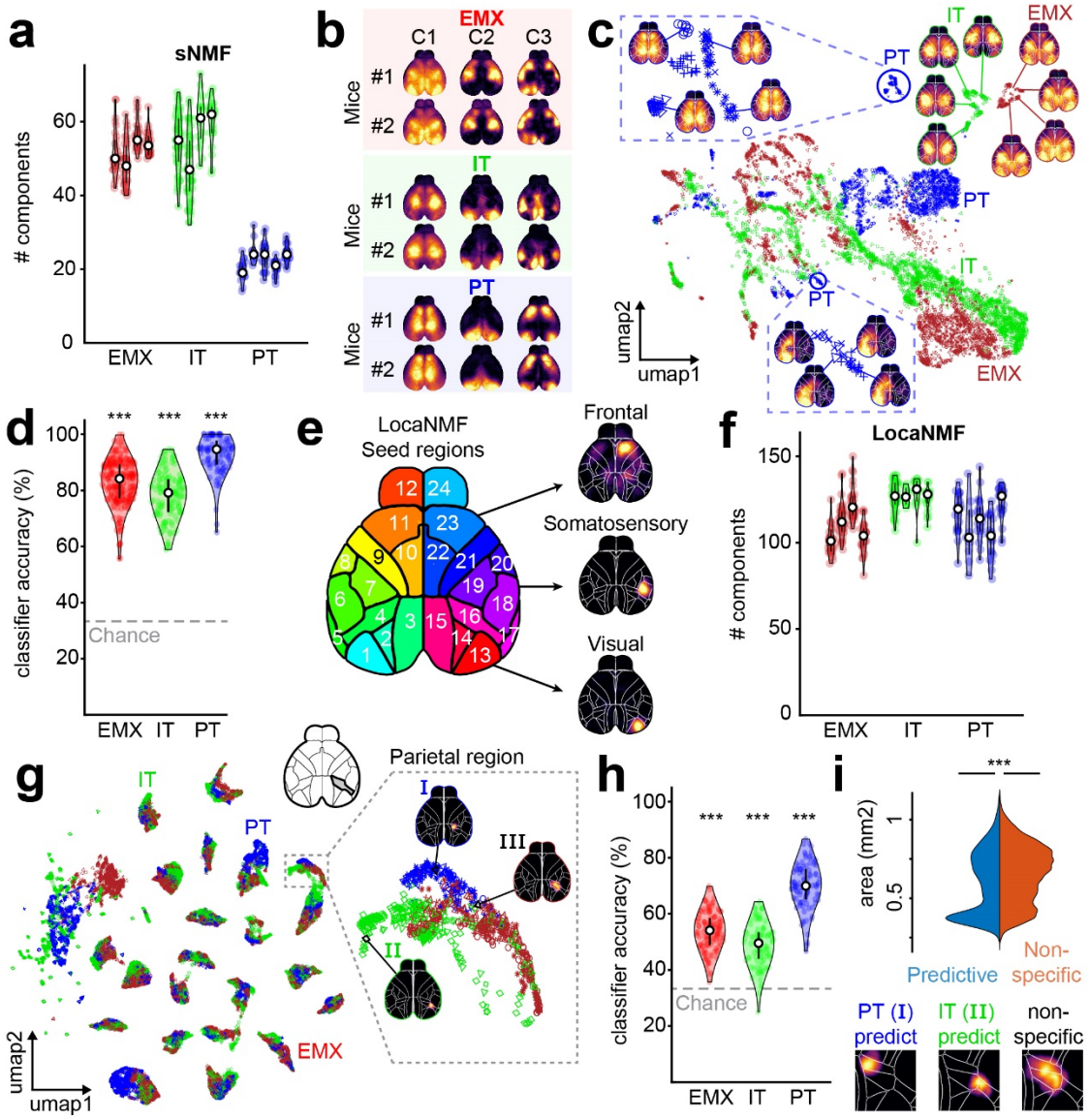

Figure 2. PyN subtypes exhibit unique cortical activity patterns.
a) Number of sNMF components accounting for 99% of cortical variance in each PyN type. Violin plots show individual mice, dots represent individual sessions. **b)** Examples of spatial sNMF components. Components from different mice from the same PyN subtype (colored rectangles) strongly resembled each other. **c)** UMAP embedding of spatial sNMF components for EMX (red), IT (green) and PT (blue) mice. Maps show example spatial components for each type and their respective UMAP locations. Different markers denote individual mice. Blow-ups show examples of PT-specific regions. Additional clustering for individual mice is sometimes evident (top left region), but was generally weaker than PyN-specific clustering. **d)** Accuracy of a PyN type classifier based on neighbor identity of individual components in UMAP space. Each data point represents the mean classification accuracy over all components in one session. **e)** Map of seed regions used for LocaNMF analysis. Example spatial components are compact and mostly confined to the appropriate seed region. **f)** Number of LocaNMF components, accounting for 99% of cortical variance in each PyN type. Conventions as in (a). **g)** UMAP projection embedding of spatial LocaNMF components. Conventions as in (c). Left: UMAP shows clustering of LocaNMF components from similar regions (same 24 regions as shown in e). Right: Components within individual regions are further divided for

different PyN types. Maps show example LocaNMF components (I-III). **h)** Accuracy of a PyN type classifier, based on individual LocaNMF components. Conventions as in (d). **i)** Top: Peak normalized distributions of area size for PyN-type-predictive (blue) versus unspecific (red) LocaNMF components. PyN-predictive components are smaller than unspecific components (PyN-predictive: median = 0.59 mm^2, n = 6317 components, nonspecific: median = 0.68mm^2, n = 18938 components; ranksum test: $p < 10^{-10}$). Bottom: Examples of PyN-predictive (I, II) and unspecific (III) components in right parietal cortex.

Since PT neurons are a subset of EMX neurons, their lower dimensionality could indicate that PT components are also a subset of EMX components. We therefore quantified to which extent components from different PyN types are linearly overlapping or independent from each other. For each PyN type, we computed the amount of variance that could be explained with components from other mice of either the same or different PyN type (Supp. Fig. 3a). For all groups, components from a similar PyN type explained significantly more variance (ΔR^2) than the maximal amount that could be explained by other types (EMX, mean $\Delta R^2 = 3.3\%$, *t*-test: $p < 10^{-10}$; IT, mean $\Delta R^2 = 1.5\%$, $p < 10^{-10}$; PT, mean $\Delta R^2 = 1.2\%$, $p < 10^{-10}$). Each group therefore contains additional PyN-type-specific variance that is independent from other types. This was also visible in reconstructed data: PT components captured larger fluctuations in IT activity (Supp. Movie 4) but failed to represent spatial details in the cortical activity patterns (Supp. Fig. 3b). Despite the similar dimensionality of IT and EMX activity (Fig. 2a), EMX ΔR^2 was also similar for IT and PT components ($\Delta R^2_{EMX\text{-}IT} = 3.4\%$, $\Delta R^2_{EMX\text{-}PT} = 3.3\%$, $p = 0.1$), demonstrating that EMX data was not largely dominated by either IT or PT neurons.

To directly compare spatial activity patterns, we then focused on spatial sNMF components. Spatial components represent cortex-wide maps of positively correlated areas and we wondered whether these correlation patterns would differ between PyN subtypes. Indeed, individual spatial components from different mice of the same PyN subtype often strongly resembled each other but differed from other PyN subtypes (Fig. 2b). To assess if most spatial components (or only a small subset) was PyN-type-specific, we performed a UMAP projection of the first 20 components from all recordings and PyN types, non-linearly embedding the pixels of each component in a 2-dimensional space (Fig. 2c)[35]. If neural activity in PT, IT and EMX mice tended to exhibit similar correlation patterns, these spatial components would be mixed together. Instead, in agreement with the notion that components of the same PyN type resembled each other, we found that components formed clusters that were largely dominated by either PT or IT neurons (green/blue markers). EMX neurons formed a third set of non-overlapping clusters, likely reflecting the combined cortical dynamics from diverse PyN types beyond PT and IT neurons that were contained in this larger group (red markers). A simple classifier reliably identified each group, based on the nearest neighbors in a UMAP projection that was exclusively based on data from other animals. Remarkably, prediction accuracy was high even when the classification was based on just a single spatial component (Fig. 2d). The presence of such clear clusters is striking given that the spatial components used in the analysis were pooled over many sessions and mice. This confirms that UMAP clusters reflect consistent PyN-type-specific activity patterns, rather than idiosyncratic differences within individual sessions or mice. Taken together, these results clearly demonstrate that PyN types differ in the complexity of cortical dynamics, contain independent variance, and exhibit unique cortex-wide correlation patterns.

An important concern is that variations in the density of Cre expression in each mouse line could result in non-uniform GCaMP expression patterns which might contribute to PyN-specific spatial components. However, GCaMP-related fluorescence was largely uniform across cortex in all mice and we observed no clear relationship between raw widefield fluorescence patterns and PyN-specific spatial components (Supp. Fig. 4a, b). Moreover, despite some fluctuations in the density of Cre-expressing neurons across areas in both mouse lines, Cre-expression patterns did not account for spatial components or specific differences between PyN types (Supp. Fig. 4c, d).

196 Nevertheless, particularly distinct activity of each PyN type in specific cortical areas could lead
197 to cortex-wide correlation patterns that are either dominated by highly active areas or where
198 inactive areas are 'missing'. In this case, the relatively low dimensionality of PT neurons might
199 be due to a lower number of active cortical areas. We therefore used a localized form of sNMF
200 (LocaNMF)[33] which extracts components that are dense and spatially restricted to a specific
201 cortical "seed" region (Fig. 2e). Analyzing LocaNMF components therefore allowed us to reveal
202 if PyN-specific differences mostly occur on a cortex-wide level (reflecting the interactions
203 between cortical areas) or further extend to the local level of individual cortical areas (e.g. due to
204 PyN-specific differences in the shape and localization of cortical areas).
205
206 First, we again compared the number of components required to explain at least 99% of the
207 variance in each PyN type. As expected, the number of components was greater than sNMF and,
208 interestingly, was also more similar across PyN subtypes (Fig. 2f). This shows that PyN-type-
209 specific differences in cortex-wide correlation patterns are not due to a lack of activity in some
210 cortical areas (which would have resulted in a lower number of required components, e.g. in PT
211 mice) and instead result from PyN-type specific differences in the coordinated activation of
212 multi-area cortical networks. Moreover, as with sNMF components, LocaNMF components from
213 mice of the same PyN type explained more variance than components from other types (Supp.
214 Fig. 3c).
215
216 Repeating the UMAP embedding for these local components also uncovered PyN-type-specific
217 clustering (Fig. 2g), which could be used to accurately identify each PyN type (Fig. 2h).
218 Classification accuracy was high across most cortical regions (Supp. Fig. 4d). Specificity of
219 LocaNMF components could either be due to the presence of specific 'subregions', where PyN
220 types are most active in smaller parts of a given cortical area, or larger 'superregions', where the
221 activity of a specific PyN type extends across known area borders. We therefore compared the
222 size of LocaNMF components that accurately predicted their respective PyN type (classifier
223 accuracy > 99%) versus nonspecific components. Interestingly, PyN-predictive clusters were
224 significantly smaller than nonspecific clusters (Fig. 2i), suggesting that different PyNs might be
225 most active in distinct subregions instead of larger multi-area components. This indicates that
226 smaller, PyN-specific subregions may reside within the coarser, traditionally-defined cortical
227 areas.

228 We next assessed how cortical dynamics of PyN subpopulations are related to decision-making
229 by imaging PyN subtype activity in animals trained on an auditory decision-making task (Fig.
230 3a)[36]. Mice initiated trials by touching small handles, which triggered the simultaneous
231 presentation of sequences of clicking sounds to their left and right side. After a short delay
232 period, mice reported decisions by licking one of two water spouts and were rewarded for
233 choosing the side where more clicks were presented. To reduce temporal correlations between
234 task events, such as trial initiation and stimulus onset, the durations of the initiation, stimulus and
235 delay periods were randomly varied across trials. In all mice, decisions varied systematically
236 with stimulus strength (Fig. 3b) and were equally affected by click sounds throughout the
237 stimulus period (Supp. Fig. 5).

238 As with spatial components, trial-averaged temporal sNMF and LocaNMF components showed
239 pronounced clustering, suggesting that different PyN-types also exhibit distinct task-related
240 temporal dynamics (Supp. Fig. 6). Correspondingly, we found clear differences in trial-averaged
241 neural activity between PyN subtypes, especially during stimulus presentation (Fig. 3c). Here,
242 cortical activity was uniformly suppressed in EMX mice, partially suppressed in somatosensory
243 and visual areas in IT mice, and uniformly increased in PT mice (Fig. 3d). In all PyN types,

activity was largely symmetric across the left and right hemispheres, even when only analyzing trials where stimuli were presented on the left side and the animal made a corresponding leftward choice (Fig. 3c; Supp. Fig. 7). Moreover, responses to sensory stimuli were much weaker than movement-related responses, such as trial initiation or licking (Fig. 3d, gray bar versus dashed lines). A potential explanation is that lateralized, task-related activity is obscured by cortical activity due to animal movements[32,37–39].

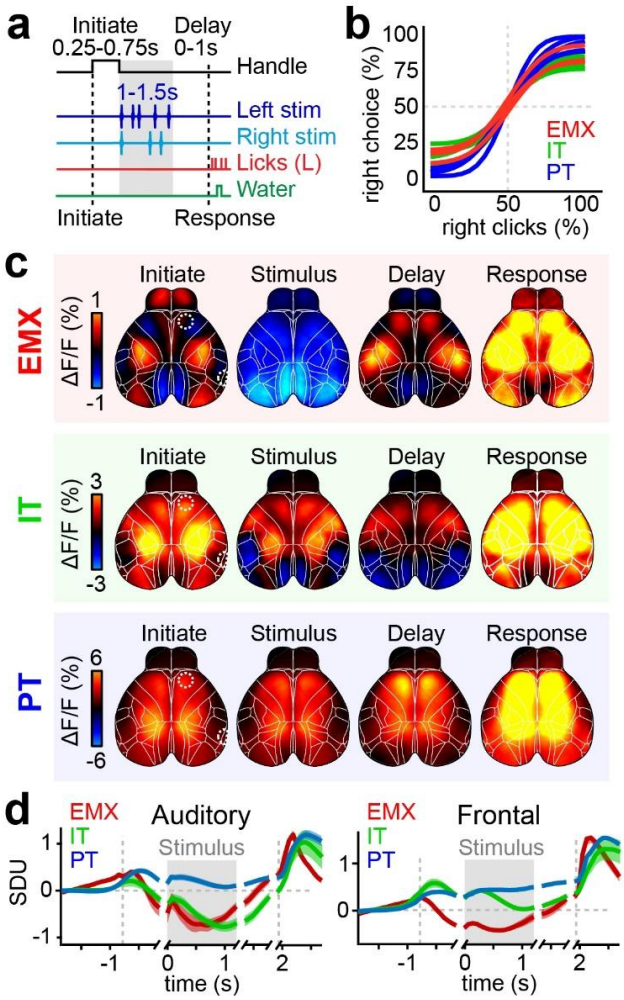

Figure 3. An auditory decision-making task reveals distinct functional activity patterns in each PyN type. **a)** Auditory discrimination task structure of an example trial. Mice touched paw handles to initiate randomized click sequences on the left and/or right side. After a delay period, a lick response on the correct side was rewarded with water. The episode duration was randomly varied in individual trials. **b)** Psychometric functions fit to behavioral data from the discrimination task in (a) of individual EMX (red), IT (green) and PT (blue) mice. **c)** Trial-averaged response maps for all correct, leftward trials in different PyN types. Shown are averages for the 'Initiation', 'Stimulus', 'Delay' and 'Response' periods shown in (a). **d)** Averaged activity in auditory (left) and frontal cortex (right) for each PyN type. Averages were separately aligned to each of the four trial periods, indicated by short gaps. Left dashed line: time of initiation, gray box: stimulus presentation, right dashed line: animal's response. Traces show standard deviation units (SDU). White dashed circles in (c) show respective area locations. Colors as in (b). Shading shows s.e.m.; n = 4 EMX/IT mice and 5 PT mice.

To isolate task-related activity from movements we used a linear encoding model[32]. The model combines many task- and movement-variables to predict single-trial fluctuations in cortical activity (Fig. 4a, top). Task variables were related to the learned behavior, and included past and

current choices, and the presentation of a sensory stimulus. Movement variables included licking and touching the handles, alongside facial movements (whisking or nose movements) obtained from two video cameras of the animal's face and body (a complete list of all task- and movement variables is shown in Supp. Table 1). All variables were combined into a single design matrix and we used ridge regression to fit the model to the imaging data. This produced a time-varying event kernel for each variable, allowing us to isolate how specific task variables (e.g. the sensory stimulus, Fig. 4a, bottom) are related to neural activity while separating them from the impact of other factors, such as licking movements, which are captured by other model variables.

To assess how well the model predicts cortical activity, we first computed the tenfold cross-validated R^2 (cvR^2). For all PyN types, the model successfully captured a large fraction of single-trial variance throughout the cortex (Fig. 4b), confirming the validity of our approach. Predicted variance was higher in IT and PT mice compared to EMX mice, with over 90% explained variance in frontal cortex of PT mice. Consistent with earlier results[32,37], movements consistently captured more variance than task variables across all PyNs (Fig. 4c). The impact of movements was also apparent when computing the unique contributions from movement or task variables by removing either set of variables from the full model, demonstrating that movements are an important driver of cortex-wide activity in all PyN types (Supp. Fig. 8a). Interestingly, unique contributions of many task variables were higher for IT, further indicating that they might be more functionally diverse than PT neurons (Supp. Fig. 8b).

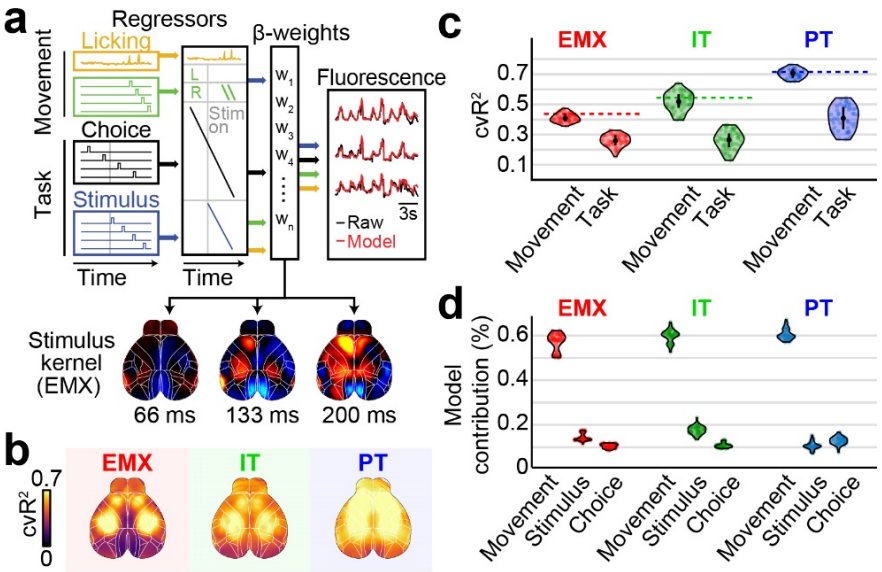

Figure 4. An encoding model uncovers task-specific differences across PyN types.
a) Schematic of the encoding model. Top: Task- and movement-variables account for fluctuations in cortical activity. Bottom: Weights for each variable define a spatiotemporal event kernel, revealing cortical activity in response to a specific event (example shows right stimulus kernel in EMX mice). **b)** Average maps of cvR^2. The model accurately predicted cortical variance for all PyNs. **c)** cvR^2 from two models, using only movement ('Movement') or task variables ('Task'). In all groups, movements were more predictive than task variables and accounted for the majority of the full models explained variance (dashed lines). Circles denote sessions. **d)** Contributions of movements, stimulus and choice to the model's total explained variance. Although movements contributed the most, stimulus and choice also made sizable contributions.

To gain insight into the cortical dynamics related to stimulus and choice, we focused on their respective event kernels learned by the model for each PyN type. To ensure that both task variables still accounted for a sizable amount of the observed neural activity (instead of all variance being explained by movements), we first computed how much variance the stimulus and choice kernels contribute to the full model compared to the sum of all movement variables

(Fig. 4d). Here, although the combined movement variables made the largest contributions (~60% of the model's total explained variance), both stimulus and choice also made sizable contributions to the model (10-20% explained variance in all PyN types). This demonstrates that stimulus and choice remain important for understanding cortical activity patterns and can be leveraged to selectively isolate task-related activity.

We then focused on cortical responses to the auditory stimulus. In contrast to trial averages of ΔF/F (Fig. 3c), the stimulus kernels in EMX mice uncovered clear sensory-locked and lateralized responses in auditory, parietal and frontal cortex (Fig. 4a, bottom; Fig. 5a, top). Other areas, such as somatosensory and visual cortex, were inhibited. Sensory-locked responses were also present in auditory, parietal and frontal cortices of PT and IT mice (Fig. 5a, center and bottom). However, the cortex-wide response patterns were not identical: for instance, no inhibition was apparent in PT mice. Sensory responses were particularly distinct in the parietal cortex (Fig. 5b). Responses in EMX and IT mice were more anterolateral in parietal area A while PT responses were surprisingly prominent and more posteromedial at the border between area AM and RS.

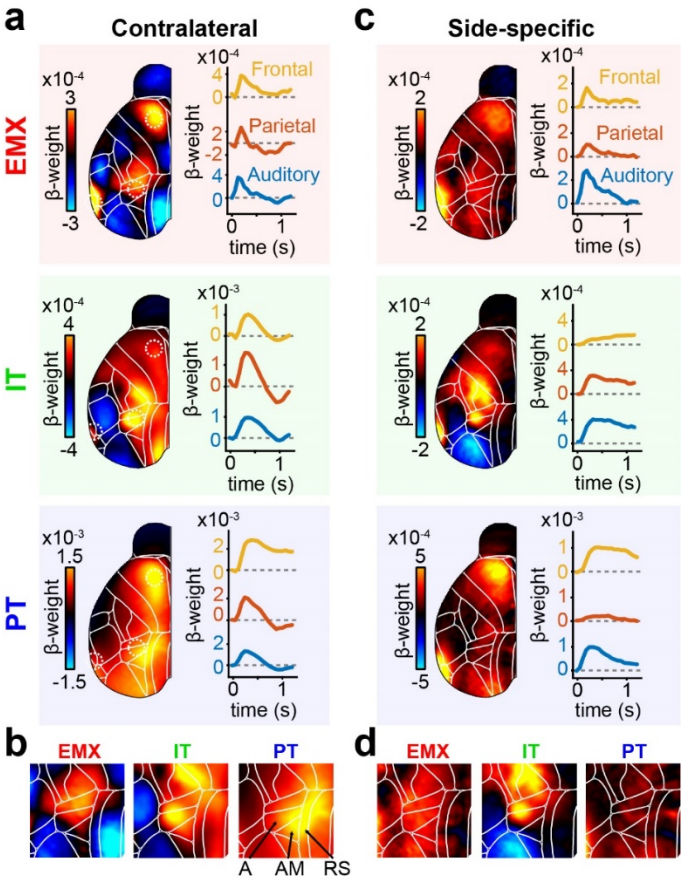

Figure 5. PyN-specific differences are evident in the location and specificity of cortical stimulus responses. **a)** Left: Response kernels for contralateral stimuli over all EMX (red), IT (green), and PT mice (blue), averaged between 0 and 200 ms. Right: Stimulus-evoked activity in auditory (blue), parietal (red), and frontal cortex (yellow). Dashed circles in the left stimulus maps show locations of respective cortical areas. **b)** Magnified view on parietal regions of the stimulus maps in (a). PyNs differed in the location of sensory responses. Arrows show location of parietal areas A, AM and the RS. **c)** Side-specific stimulus responses, computed as the difference between contra- and ipsilateral stimulus kernels. Conventions as in (a). **d)** Magnified view on parietal regions of side-specific maps in (c). IT neurons show clear, side-specific responses that were weaker in EMX and absent for PT neurons.

PyN types also differed in their response dynamics following the sensory stimulus. While some cortical areas, such as auditory cortex, preferentially responded to contralateral stimuli, PT

325 neurons in parietal cortex were activated bilaterally in response to ipsi- or contralateral stimuli.
326 To assess such side-specificity, we computed the difference between the contra- and ipsilateral
327 stimulus kernels (Fig. 5c, colors indicate regions for which responses differed for contra- versus
328 ipsilateral stimulus kernels). In EMX mice, we found lateralized responses in auditory, frontal,
329 and to a lesser extent, parietal cortex (Fig. 5c,d). Lateralized IT activity was found in auditory
330 and parietal but not frontal cortex. In contrast, PT mice showed clear side-specific responses in
331 auditory and frontal but not in parietal cortex. Such differences in unilateral versus bilateral
332 responses in PT and IT neurons may also reflect different functional roles, with unilateral
333 responses encoding the spatial location of sensory information and bilateral responses signaling
334 its importance for guiding subsequent decisions.

335 Having identified PyN-type dependent activity for sensory stimuli, we then examined choice-
336 dependent activity and again observed clear differences across PyN types. In EMX mice, a
337 number of regions showed choice-related activity, particularly in the frontal cortex, while
338 sensory and parietal regions were only weakly modulated (Fig. 6a). We also found choice signals
339 in somatosensory areas of the whiskers and nose that slowly increased over the course of the
340 trial, even before the stimulus onset (Supp. Fig. 9a). These signals could indicate that mice used
341 their whiskers to probe the location of the spouts or performed subtle, choice-predictive facial
342 movements throughout the trial[40]. In contrast, choice-specific activity in frontal cortex strongly
343 increased after stimulus onset and remained elevated as the decision progressed from sampling
344 the stimulus to the subsequent delay period (Fig. 6a, yellow trace). We found equally prominent
345 choice signals in frontal cortex of PT mice while little choice-predictive activity was seen in IT
346 mice (Fig. 6b, Supp. Fig. 9b,c). In EMX and PT mice, positive signals for contralateral choices
347 were concentrated in the medial part of secondary motor cortex (M2) while parts of the primary
348 motor cortex (M1) were inhibited. This could indicate accumulation of sensory evidence and
349 motor preparation in M2, and inhibition in parts of M1 when early lick responses must be
350 witheld[41].

351 Although the choice kernels revealed differences between PyN types, choice-related activity only
352 accounted for a small amount of the total neural variance (Fig. 4d, Supp. Fig. 8). Since the
353 encoding model is designed to capture as much variance as possible, we hypothesized that this
354 approach might miss subtle choice signals that are specific but low in magnitude. The linear
355 model's ridge penalty also enforces choice-related variance to be distributed over all correlated
356 model variables, which might 'diffuse' weaker choice-related activity from the choice to other
357 model kernels.

358 To selectively isolate all choice-related activity, we therefore built a decoding model, using a
359 logistic regression choice classifier with L1 penalty (see Methods). In contrast to the encoding
360 model, this decoder approach isolates the cortical signals that are best suited to predict the
361 animal's choices, regardless of their magnitude. For all PyN types, the decoder predicted the
362 animal's choices with high accuracy, confirming that cortical activity reliably reflects trial-by-
363 trial choices (Supp. Fig. 10a). When analyzing the decoder weights, we found comparable
364 patterns to the encoding model's choice kernels but with much clearer separation of cortical
365 areas (compare top row 'Delay' in Fig. 6c to Fig. 6a, left). Here, positive decoder weights denote
366 areas that are most predictive for contralateral choices but, importantly, this does not suggest that
367 these areas are necessarily the most active. For all PyN types, we found significant choice signals
368 in multiple areas of the anterior cortex that evolved during decisions (Fig. 6c, Supp. Figs. 10,
369 11). In EMX and PT mice (top and bottom rows), large parts of M2 were again highly choice
370 predictive, including the anterior lateral motor cortex (ALM) and the medial motor cortex
371 (MM)[21]. M2 choice weights strongly increased immediately after stimulus onset and remained
372 elevated during the subsequent delay period (Fig. 6c,d). Cortical choice signals also persisted

after removing movement-related activity from the data, suggesting that they are not explained by choice-predictive animal movements but instead reflect the formation of sensory-driven decisions in frontal cortex (Supp. Fig. 12).

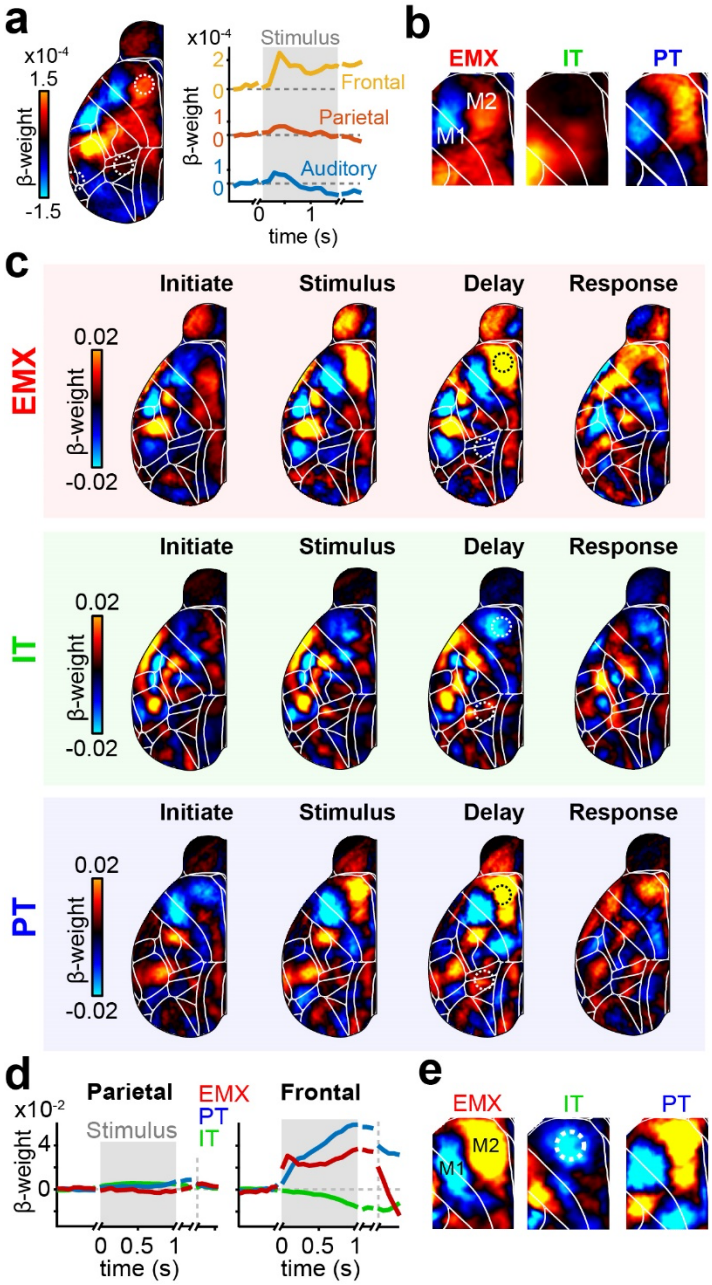

Figure 6. The temporal dynamics of choice-related activity differ across PyN types.
a) Left: Averaged choice kernels for EMX mice during the delay period. Positive weights indicate increased activity for contralateral choices, negative weights indicate choice-related reduction in activity. Right: Choice-related activity in auditory (blue), parietal (red), and frontal cortex (yellow). Traces are re-aligned to the initiation, stimulus, delay and response periods, indicated by gaps in weight traces. **b)** Zoomed-in map for frontal choice kernels of EMX, IT and PT mice during the delay period. **c)** Cortical maps of contralateral choice weights for different trial episodes. Several areas in anterior cortex showed clear choice signals. **d)** Baseline-corrected decoder weights in parietal (left) and frontal cortex (right) throughout the trial. Conventions as in (a). Dashed circles in the delay maps of (c) show the parietal and frontal locations that were used to compute the traces. **e)** Zoomed-in map for frontal decoder weights of EMX, IT and PT mice during the delay period. Dashed circle shows location of ALM.

387 Surprisingly, we also found a mild ipsilateral choice-preference for M2 in IT mice, despite strong
388 bilateral activation of frontal cortex during the delay period (Fig. 3c; Supp. Fig. 7). This
389 ipsilateral choice signal evolved more slowly during the stimulus and delay period (Fig. 6c,d)
390 and was more spatially restricted to ALM (Fig. 6e). In line with our previous results, no choice
391 signals were seen in parietal cortex of any PyN type (Fig. 6d, left), suggesting that parietal cortex
392 is mostly involved in sensory processing instead of choice formation or motor execution[42,43].

393 Compared to the encoding model, the decoding model recovered more finely structured choice
394 maps, especially in the frontal regions (compare Fig. 6e to 6b), revealing strong contralateral
395 choice signals in PT and ipsilateral choice signals in IT mice. One possible cause of this
396 unexpected inversion may be different choice-selectivity of specific IT-subtypes: intracortical
397 versus corticostriatal (CStr) projection neurons. Earlier work suggested an even distribution of
398 ipsi- and contralateral choice selectivity in frontal intracortical projection neurons[20,21], and we
399 thus hypothesized that our observed IT choice selectivity is due to the activity of CStr neurons.
400 To address this directly, we used an intersectional approach that exclusively labels large
401 populations of CStr neurons by performing multiple bilateral striatal injections of a retrograde
402 virus expressing Cre (CAV2-Cre) in GCaMP6s reporter mice (Fig. 7a), inducing widespread
403 expression in CStr neurons (Fig. 7b). As expected, GCaMP6 expression in CStr neurons was
404 largely confined to layer 5 with sparse expression in deeper layers.

405 We then used widefield calcium imaging to selectively measure activity from CStr neurons. As
406 with PT and IT mice, we observed robust fluorescence signals throughout the dorsal cortex
407 (Supp. Movie 5) and identified visual areas using retinotopic mapping (Supp. Fig. 13a). sNMF
408 showed that the dimensionality of CStr mice was intermediate between PT and IT activity, and
409 that the spatial components did not strongly overlap with other PyN types (Supp. Fig. 13b,c).
410 This clear difference between IT and CStr mice strongly suggests that imaging signals from IT
411 mice are not solely dominated by IT-positive CStr neurons but represent a mixture of
412 intracortical- and corticostriatal-projecting IT neurons with distinct activity patterns.

413 We then trained CStr mice in the auditory discrimination task. Trial-averaged dynamics partially
414 resembled IT mice, for example in frontal cortex, but also showed clear differences, such as a
415 lack of pre-stimulus suppression in sensory cortex (Fig. 7c,d; orange versus gray traces).
416 Differences between CStr and IT mice were also visible in the stimulus kernels from the
417 encoding model. In CStr mice, stimulus-related activity in parietal cortex was stronger than in
418 sensory and frontal cortex but the activated parietal regions were more medial than in IT mice
419 (Fig. 7e). Interestingly, these stimulus-driven parietal regions (Fig. 7f, top) closely resembled
420 cortical areas that form anatomical and functional connections to the dorsomedial striatum[44,45].
421 As with PT neurons (Fig. 5b,d), parietal CStr responses equally responded to contra- and
422 ipsilateral stimulation (Fig. 7f, bottom).

423 To determine whether CStr activity contributed to ipsilateral-preferring IT choice signals, we
424 repeated the choice decoder analysis. The decoder predicted animals' choices with equally high
425 accuracy as for PT and IT mice (Supp. Fig. 13d). We then extracted choice weights for each task
426 episode. Here, CStr activity was overall similar to that of IT mice, with an even stronger
427 ipsilateral-choice preference in frontal cortex that started after stimulus onset and lasted
428 throughout the delay and response periods (Fig. 7g, right). As in IT mice, this inversion from
429 contra- to ipsilateral choice preference was prominent in area ALM but did not extend to MM,
430 strongly suggesting that ipsilateral choice preference is driven by IT-CStr neurons.

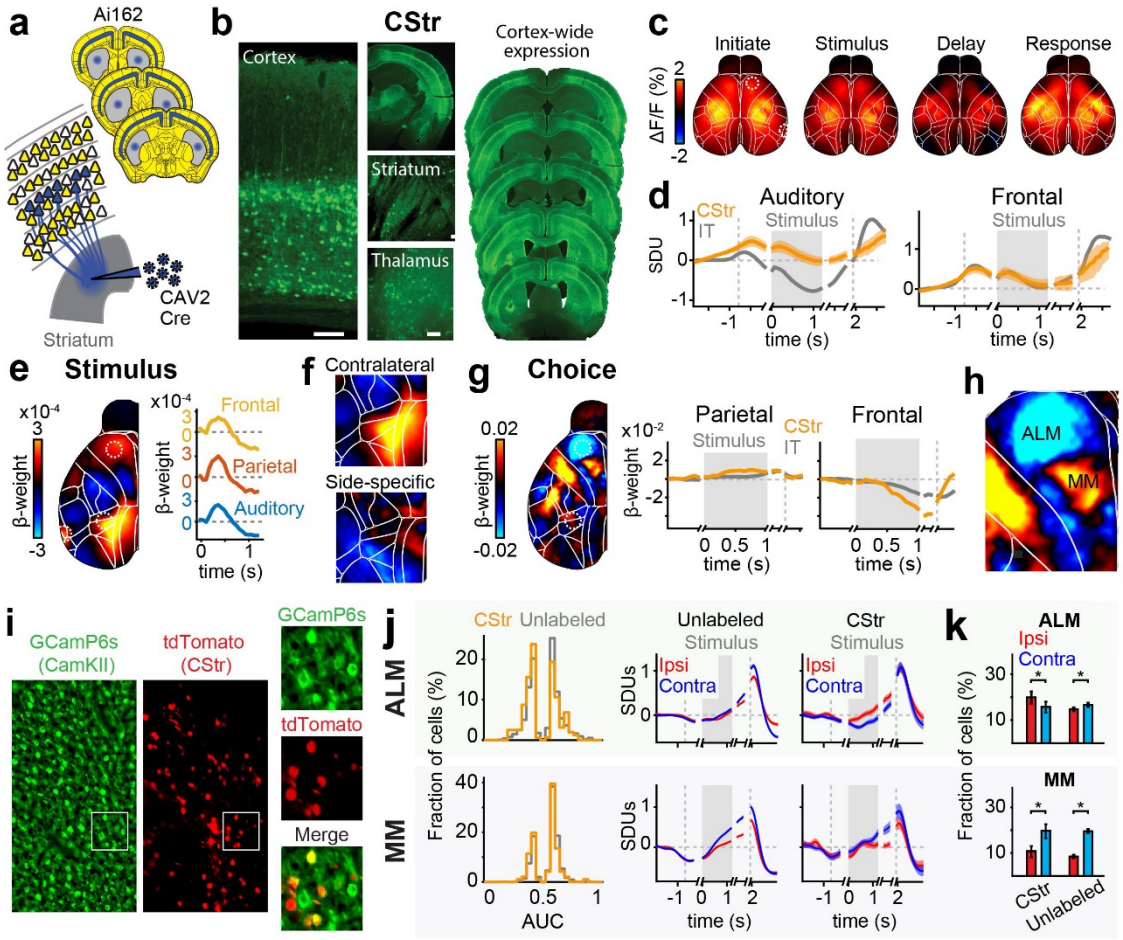

Figure 7. An intersectional approach to measure cortex-wide activity of CStr neurons.
a) Schematic of the retrograde labeling approach. Multiple bilateral injections of retrograde CAV2-Cre virus in reporter mice robustly induced expression of GCaMP6s in CStr neurons. **b)** Left: GCaMP6s-expression was robust throughout the dorsal cortex. Scale bars are 100 µm. Right: Brain slices show robust cortex-wide expression. **c)** Cortical dynamics of CStr neurons in the auditory discrimination task. Shown are trial-averages over all correct, leftward trials in different trial episodes. No clear lateralization was observed in trial averages. **d)** Averaged activity in auditory (left) and frontal cortex (right) for CStr (orange) and IT (gray) mice. Dashed lines show times of initiation and response periods, gray areas the stimulus period. Traces show standard deviation units (SDU). **e)** Left: Contralateral stimulus kernel, averaged over all CStr mice, between 0 and 200 ms after stimulus onset. Right: Colored traces show changes in sensory (blue), parietal (red) and frontal cortex (yellow). Locations for each area are indicated by dashed circles in the weight map. **f)** Top: Weight map from (e), zoomed in on parietal cortex. Bottom: Difference of contra- versus ipsilateral stimulus kernels. **g)** Left: Cortical weight map from choice decoder during the delay period, averaged over all CStr mice. Right: Baseline-corrected decoder weights in parietal (left) and frontal cortex (right) for CStr (orange) and IT mice (gray). Traces are re-aligned to the initiation, stimulus, delay and response periods, indicated by gaps in weight traces. **h)** Weight map from (g), zoomed in on frontal cortex. **i)** Example field-of-view from two-photon imaging. Left panel: GCaMP6s-expression in all PyNs (green). Center panel: retrogradely-labeled CStr neurons, expressing tdTomato (red). Right panels: zoomed-in maps for both channels and a merged image. **j)** Left: Overview of significantly choice-tuned neurons in ALM (top) and MM (bottom), imaged between 200-400 µm. Orange line shows CStr neurons, gray lines are unlabeled PyNs. AUC values below 0.5 indicate stronger responses for ipsilateral choices. Right: Trial-averaged activity for all choice-selective neurons, separated for ipsi- (red) versus contralateral choices (blue). CStr neurons in ALM (top right) show higher activity for ipsilateral choices. **k)** Fraction of cells responding selectively for ipsi- versus contralateral choices. Top: A higher fraction of CStr neurons in ALM are ipsi-selective ($CStr_{Ipsi}$: 20.4%, $CStr_{Contra}$: 15.5%, binomial test: $p = 0.0018$) while unlabeled neurons are more contra-selective ($Unlabeled_{Ipsi}$: 14.3%, $Unlabeled_{Contra}$: 17.2%, binomial test: $p = 3.5\text{x}10^{-10}$). Bottom: The majority of CStr as well as unlabeled neurons in MM are selective for contralateral choices ($CStr_{Ipsi}$: 10.2%, $CStr_{Contra}$: 19.1%, binomial test: $p = 2.7\text{x}10^{-8}$; $Unlabeled_{Ipsi}$: 9.3%, $Unlabeled_{Contra}$: 19.6%, binomial test: $p < 1\text{x}10^{-10}$).

459 To confirm these results on a single-cell level, we then used two-photon calcium imaging in
460 Camk2α-tTA;G6s2 mice and labeled CStr neurons through striatal injections of a retrograde
461 adeno-associated virus (AAVrg-tdTomato) (Fig. 7i). This allowed us to compare the activity of
462 all PyNs in frontal cortex with tdTomato-labeled CStr neurons in the same animal. Comparing
463 the choice-tuning of CStr and unlabeled PyNs revealed a specific difference in ipsi- versus
464 contralateral choice preference in ALM (Fig. 7j). Here, significantly more choice-selective CStr
465 neurons preferred ipsilateral choices, whereas unlabeled PyNs were mildly contra-selective (Fig.
466 7k). In agreement with our widefield results, these differences were only seen in ALM but not
467 MM. Interestingly, this ipsilateral choice preference was also restricted to superficial IT-CStr
468 neurons at a cortical depth between 200-400 µm. Infragranular CStr neurons (400-600 µm),
469 which are also often PT cells[17], showed strong contralateral choice tuning that was similar to
470 unlabeled cells (Supp. Fig. 14a). Lastly, we also tested if the neuropil exhibits distinct choice
471 signals that may have masked somatic activity in our PyN-specific widefield measures (Supp.
472 Fig. 14b). In all regions and depths, neuropil choice tuning was largely similar to somatic activity
473 of unlabeled neurons, confirming that widefield measures indeed represented local somatic
474 activity. Here, IT-specific widefield signals matched the mixed choice-selectivity of superficial
475 layers, while PT-specific imaging was well-aligned with the clear contralateral choice tuning in
476 deeper cortical layers.

477 The observed differences between PyN types suggest that each type may drive distinct aspects of
478 decision-making. To causally test the functional role of different PyN types, we performed PyN-
479 specific optogenetic inactivation in different cortical areas. We induced Cre-dependent
480 expression of the inhibitory opsin stGtACR2[46] by injecting an AAV in the parietal and frontal
481 cortex of Fezf2-, PlexinD1-, or EMX-Cre mice (Fig. 8a, b, Supp. Table 2). To express stGtACR2
482 in CStr neurons, we used a combined viral receptor complementation and intersectional approach
483 to maximize the efficiency of retrograde expression[47]. First, we simultaneously expressed the
484 coxsackievirus and adenovirus receptor (CAR) and transduced Cre-dependent stGtACR2 in
485 cortical neurons. Two weeks later, we performed retrograde-mediated stGtACR2 expression
486 through striatal CAV2-Cre injections. CAR mediates efficient axonal uptake of CAV2 and
487 prevents potential viral tropism in subsets of CStr neurons. The coordinates of auditory, parietal,
488 and frontal injections and subsequent inactivation were determined from our stimulus and choice
489 analyses (Fig. 5a, 6a; dashed circles). To test whether optogenetic effects are area-specific, we
490 also targeted the primary visual cortex (V1) in a subset of EMX mice as controls. To simplify the
491 behavioral task during the optogenetic inactivation experiments, we only presented unilateral
492 stimuli in each trial and kept the stimulus duration and delay periods constant (1 and 0.5 seconds,
493 respectively).

494 In agreement with our imaging results, bilateral optogenetic inactivation of auditory, parietal or
495 frontal cortex of EMX mice strongly impaired auditory decision accuracy (Fig. 8c). Performance
496 was unaffected by V1 inactivation, confirming that these areas are selectively required for
497 auditory decisions. We then illuminated each area for 0.5 seconds during four different task
498 episodes: Early and late stimulus (the first and last 0.5 seconds of the stimulus period), delay and
499 response (Fig. 8d). In agreement with our observation that auditory and parietal cortex reflects
500 stimulus driven activity (Fig. 5a, red and blue traces), inactivation of either area strongly reduced
501 animal's performance, particularly during the stimulus period (Fig. 8e, f). Behavioral
502 impairments (computed as the normalized difference between performance in non-optogenetic
503 trials and chance) were weaker during the subsequent trial periods, indicating that these areas are
504 most important for early processing of auditory stimuli. As expected, impairments were strongest
505 in EMX mice where all PyNs were affected (gray trace).

In agreement with earlier work[48], inhibiting CStr neurons in A1 also affected auditory decisions (Fig. 8e, orange trace). However, the effects were more transient and weaker compared to inactivation of EMX neurons, suggesting that CStr neurons were not exclusively required for accurate task performance. This was even more evident in parietal cortex where impairments were surprisingly weak when inhibiting either IT or CStr neurons (Fig. 8f, green/orange traces) while inactivating PT neurons resulted in a more robust impairment (blue trace). This suggests that the subcortical PT projection pathways in the parietal cortex have a larger causal impact on sensory processing than intracortical IT or CStr projections, pointing to a role for PT neurons that extends beyond preparation and execution of movements.

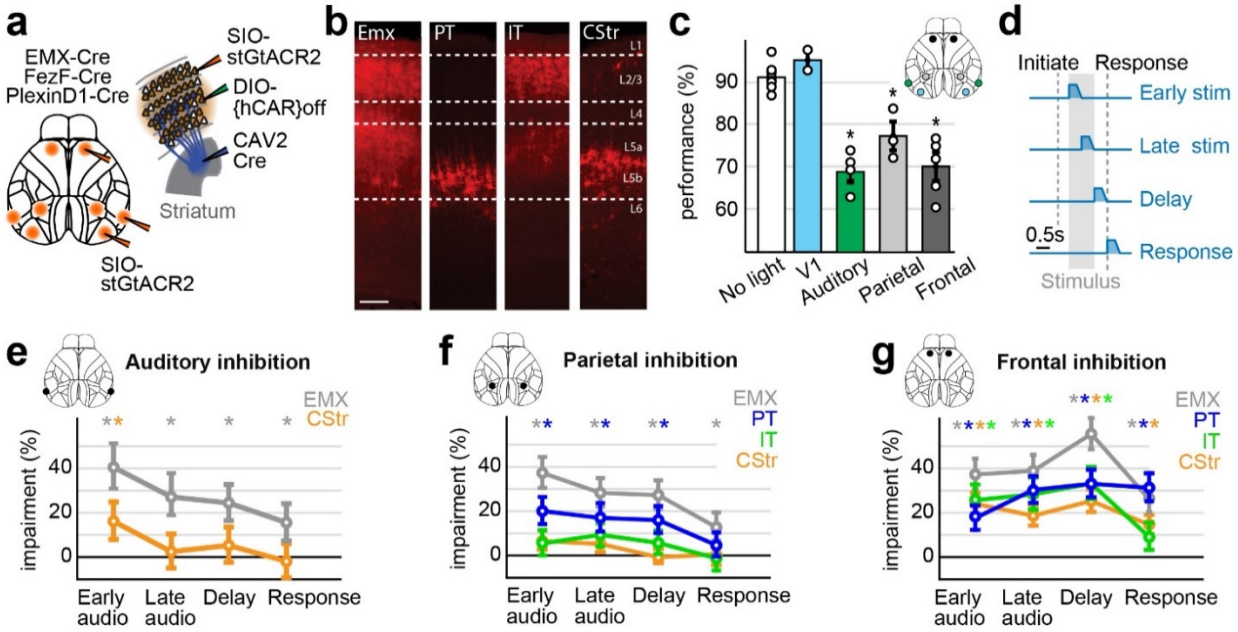

Figure 8. Temporally restricted, PyN-specific inactivation of parietal and frontal cortex disrupts decisions. **a)** Left: Schematic of injection scheme to induce stGtACR2 expression in EMX, IT, or PT neurons. Injections were performed in auditory, parietal and frontal cortex of transgenic mice to target different PyN types. V1 injections were performed in a subset of control EMX mice. Right: Intersectional viral approach for targeting CStr neurons. AAV-DJ-hSYN-DIO-hCAR{off} induced expression of CAR in cortical neurons to promote uptake of CAV2-Cre virus from the striatum. A second cortical injection induced Cre-dependent stGtACR2 expression in all CStr neurons. **b)** Layer-specific expression of stGtACR2-FusionRed in EMX, PT, IT and CStr neurons. **c)** Behavioral performance (% correct) of EMX mice during inactivation of V1, auditory, parietal or frontal cortex. Inhibition of auditory, parietal and frontal cortex, but not V1, significantly reduced task performance. Circles indicate individual mice, error bars show the s.e.m. **d)** Schematic of optogenetic inactivation paradigm. 0.5-s long optogenetic inhibition was performed during the first or last part of the stimulus period, the subsequent delay or the response period. Light power ramped down after 0.3 seconds. **e)** Behavioral impairment (% change from control performance) with inhibition of EMX or CStr neurons in auditory cortex. Circles show mean impairments, error bars 95% confidence intervals. **f)** Behavioral impairment with inhibition of different PyN types in parietal cortex. Conventions as in e). **g)** Behavioral impairment with inhibition of different PyN types in frontal cortex. Conventions as in f). Stars in all panels indicate significance (bonferroni-corrected $p < 0.01$, binomial test).

Frontal inactivation resulted in a particularly strong impairment, especially for nonspecific PyN inactivation (EMX mice, Fig. 8g, gray trace), consistent with a role for frontal cortex in sensory integration and working memory[20,43,49]. IT and CStr inactivation resulted in comparable behavioral impairments during the stimulus and delay periods (Fig. 8g, green and orange traces). Choice impairments in IT mice are therefore not solely due to the disruption of intracortical processing[20] but also involve alterations of CStr neurons. Inactivating PT neurons equally impaired animal performance during the stimulus and delay period but showed stronger effects during the final response period. Impairments in the response period were similar for EMX and

PT mice, suggesting that PT neurons are particularly involved in licking responses. These results show that multiple PyN types in frontal cortex are involved in the formation and maintenance of choices, despite clear differences in their respective choice tuning. Lastly, we also analyzed licking patterns to test if optogenetic inhibition broadly disrupted animal movements. Frontal inactivation in the delay period had a mild effect on response latency but did not affect response probability or licking patterns, arguing against a strong motor impairment (Supp. Fig. 15). This shows that PyN-specific inhibition selectively reduced the animals' response accuracy rather than broadly disrupting their ability for movement initiation and execution.

Discussion

We measured and manipulated PyN subtypes to determine whether they play distinct roles in decision-making. Cortex-wide activity patterns were PyN subtype-specific, each reflecting distinct neural dynamics at multiple spatial scales. Functional specificity across PyN subtypes was also evident during auditory decision-making: activity of each PyN subtype exhibited unique cortical localization and spatial specificity associated with stimulus and choice. These response patterns were not seen when imaging from PyNs nonspecifically. Optogenetic inactivation confirmed that PyN types in parietal and frontal cortex have distinct functional roles, highlighting the importance of subcortical projection pathways for sensory processing and choice formation. Taken together, our results suggest that different PyN types form parallel subnetworks throughout the cortex, are functionally-distinct, and perform separate roles during auditory decision-making.

Dimensionality reduction of cortical dynamics[33,50,51] revealed that nearly all spatial components were also PyN-subtype-specific. Differences between PyNs are therefore not only present within parcellated cortical regions[18–20] but also evident in large-scale activity patterns. This has important implications for studies of cortex-wide neural dynamics, which are often based on indirect measures of neural activity[52,53] or pooled activity from all PyNs[22,25,54,55]. Earlier work revealed intricate circuit motifs and functional modules that span the entire cortex[50,54–57] and largely follow intracortical connectivity patterns[58,59]. Our results point to the existence of additional circuit motifs when specific PyN population are isolated, especially subcortical projection types, such as PT or CStr neurons. Furthermore, most PyN-specific LocaNMF components consisted of spatially precise subregions that were smaller than Allen CCF areas. Detailed analysis of PyN-specific activity might therefore reveal more detailed cortical structures than could be observed with nonspecific measures. For future studies, a particularly promising approach to achieve this goal would be to combine large-scale measures of multiple PyN types with multi-color widefield imaging[24,60] and directly observe interactions between PyN-specific cortical dynamics within the same animal.

Sensory responses were pronounced in auditory, parietal and frontal cortices[42,43,61,62] and revealed unique response patterns for each PyN type. This functional segregation is in line with recent results from primary sensory areas, such as somatosensory[18,63] and visual cortex[19], and strongly suggests that different PyN types play separate roles during sensory processing. Moreover, the clear differences in magnitude, localization, and lateralization of sensory responses in parietal and frontal cortex demonstrate that the functional specialization of different PyN subtypes is a general feature of cortical circuit function.

We selectively inactivated different PyN types across cortical areas to directly test their involvement in the behavioral task. In agreement with earlier work, inhibiting CStr neurons in auditory cortex impaired task performance[48], suggesting that projections from cortex to striatum are important for accurate auditory decisions. Moreover, inactivation of parietal cortex also

586 caused strong behavioral impairments, especially during sensory stimulation. Surprisingly,
587 inactivation of CStr or IT neurons caused only weak behavioral effects. This shows that the
588 importance of CStr projections does not generalize from auditory to parietal cortex and also
589 argues against models in which task-relevant sensory information is directly transmitted from
590 parietal to frontal cortex to promote decision formation[42,62,64]. Instead, inactivation of parietal PT
591 neurons during the stimulus presentation strongly disrupted eventual decisions, highlighting the
592 importance of subcortical projection pathways for auditory performance. A likely subcortical
593 target is the SC, which receives inputs from PT neurons[18,26] and has been implicated with
594 somatosensory[18] and visual[65,66] perception, and decision-making[39,67,68].

595 The strong behavioral effects with inactivation of parietal cortex are at odds with earlier studies
596 in rats that showed very little or no impact of parietal inactivation in auditory task
597 performance[69,70]. Conversely, other work in head-fixed mice had found robust behavioral effects
598 in visual[43,71–73] and auditory[62] task performance. While a potential reason for these contradictory
599 results could be species differences between rats and mice, the precise location of parietal
600 inactivation most likely plays an important role. Different sensory modalities are processed along
601 a mediolateral gradient in parietal cortex, emphasizing the need to precisely target specific
602 parietal areas to obtain a modality-specific behavioral effect[62]. We also found that parietal
603 responses of PT and CStr neurons were located more medially than IT neurons, further
604 emphasizing the need for precise localization. Another important factor is the specific behavioral
605 task. Our task design required accumulation of sensory evidence and working memory which
606 engage a wider range of cortical regions[72] and might therefore explain the involvement of
607 parietal cortex for accurate auditory decisions.

608 The accumulation and memory requirements of the decisions we studied might also explain why
609 we found clear cortical choice signals, especially in frontal cortex, whereas recent cortex-wide
610 studies reported little choice-selectivity[39,74]. The lack of side-specific choice tuning in IT
611 population data is consistent with earlier work, showing that intracortical projection neurons in
612 frontal cortex include an equal amount of contra- and ipsilateral choice-preferring cells[20,21]. In
613 contrast to other PyNs, CStr neurons were more selective for ipsilateral choices. Using two-
614 photon imaging, we confirmed that this ipsilateral choice preference was also present in
615 individual CStr neurons but not in unlabeled IT neurons. This confirms that our PyN-specific
616 widefield results indeed reflect selective somatic activity and not just superficial neuropil signals,
617 in line with earlier findings that widefield signals are strongly correlated to spiking of cortical
618 neurons[44]. Ipsilateral choice signals in CStr neurons were restricted to superficial layers of area
619 ALM, which is mostly implicated in movement generation[13,49]. A recent study showed that CStr
620 projections from the anterior cingulate cortex can inhibit striatal activity and motor behavior[75]. A
621 potential reason for the reduced activity of CStr neurons during the response period could
622 therefore be to disinhibit striatal circuits and release a targeted licking response.

623 In agreement with our imaging results, frontal inactivation strongly impaired animal behavior
624 during the stimulus and delay period, suggesting an important role for the translation of sensory
625 inputs into behavior[21,74,76–78]. Impairments were largely similar for all frontal PyN types, which
626 appear to be equally required for choice formation and retention. Frontal PyNs may thus be more
627 reliant on each other to maintain accurate function than in sensory areas[18,19,48]. As the only
628 exception, PT neurons were more important during the response period, consistent with a
629 specific role of brainstem-projecting PT neurons for motor execution[13].

630 Our work offers a new perspective on cortex-wide dynamics by viewing them through the lens of
631 different PyN types and strongly supports the view that cortical circuits perform parallel
632 computations, even within the same cortical layer[13,18,19,79]. Future work to reveal the circuit logic

633 of cortex-wide activity patterns in different behavioral contexts should therefore include PyN
634 type information to resolve the functional heterogeneity that is often encountered when studying
635 cortical decision circuits. A powerful tool to achieve this goal are novel mouse lines, such as our
636 temporally inducible knock-in lines that allowed us to reliably target PT and IT neurons with
637 high specificity. These new mouse lines also overcome several known problems of earlier
638 transgenic approaches, unstable expression patterns across cortical areas or mixtures of cell types
639 due to interactions with surrounding genetic elements[26,80]. Future studies could explore PyN type
640 function at even higher granularity by using more specific mouse lines, such as the Cux1-line to
641 selectively isolates intracortical projection neurons[26]. Moreover, combining genetic mouse lines
642 with retrograde labeling will enable the targeting of specific PyN subtypes, such as projection-
643 specific PT neurons[12,13], that might serve a large array of functions from sensory processing, to
644 working memory and motor function[13,18].

645 **Acknowledgements**

646 We thank Z. Josh Huang for providing the Fezf2-2A-CreER and PlexinD1-2A-CreER mouse
647 line and for countless insightful conversations; Shreya Saxena and Joao Couto for technical
648 advice and scientific discussions; Anup Khanal for assistance with animal perfusions; Sandra
649 Brill, Maria Perez and Alice Despatin for animal training; Adam Kepecs for providing the viral
650 vector AAV-DJ-hSYN-DIO-hCAR{off}; Katherine S. Matho for invaluable help with Fezf2 and
651 Plexin cell density quantification. This work was supported in part by NIH grants R01EY022979
652 and W911NF-16-1-0368 as part of the collaboration between the US DOD, the UK MOD and
653 the UK Engineering and Physical Research Council under the Multidisciplinary University
654 Research Initiative to A.K.C. S.M. was funded by the Deutsche Forschungsgemeinschaft (DFG,
655 German Research Foundation) - 368482240/GRK2416 and the Helmholtz association (VH-NG-
656 1611). X.R.S. was supported by the NRSA F32 MH120888.

657 **Methods**

658 **Mouse lines**

659 All surgical and behavioral procedures conformed to the guidelines established by the National
660 Institutes of Health and were approved by the Institutional Animal Care and Use Committee of
661 Cold Spring Harbor Laboratory. Experiments were conducted with male mice between the ages of
662 8 to 25 weeks. No statistical methods were used to pre-determine sample sizes but our sample sizes
663 are similar to those reported in previous publications[22,25]. All mouse strains were acquired from
664 the Jackson Laboratory, the Allen Brain Institute, or generated at Cold Spring Harbor Laboratory.
665 Transgenic strains crossed to generate double- and triple-transgenic mice used for imaging: Emx-
666 Cre (JAX 005628), LSL-tTA (JAX 008600), Ai93D (JAX 024103), Ai162 (JAX 031562), TRE-
667 GCaMP6s (G6s2, JAX 024742) and H2B-eGFP (JAX 006069). EMX mice, used for calcium
668 imaging, were bred as Ai93D;Emx-Cre;LSL-tTA. To avoid potential aberrant cortical activity
669 patterns, EMX mice were on a doxycycline-containing diet (DOX), preventing GCaMP6s
670 expression until they were 6 weeks or older[22,25].

671 For widefield imaging of PT and IT neurons, inducible knock-in drivers Fezf2-2A-CreER and
672 PlexinD1-2A-CreER (Supp. Table 2), respectively, were crossed with Ai162 reporter mice to drive
673 cortex-wide GCaMP6s expression. Cre activity was induced through two doses of intra-peritoneal
674 injections of tamoxifen (200 mg/kg; 20 mg/ml solution dissolved in corn oil) at P28 and P32.
675 Histologic characterization revealed pyramidal neuron expression patterns consistent with prior
676 reports[26]. For widefield imaging of corticostriatal neurons, we first crossed Ai162 with G6s2 to

677 create a new double-transgenic reporter strain Ai162;G6s2 with two hemizygous copies of
678 GCaMP6s under tetO control. Since LSL-tTA is incorporated in-tandem to the reporter gene in
679 the Ai162 strain[29], this hybrid reporter line permits Cre-dependent expression of GCaMP6s at
680 higher levels than Ai162 hemizygotes while avoiding potential leaky reporter gene expression that
681 is sometimes found in Ai162 homozygotes. Next, to achieve widespread GCaMP6s expression in
682 corticostriatal neurons, we performed striatal injections of retrograde virus (CAV2-Cre) in the
683 hybrid Ai162;G6s2 reporter line (see section: viral injections).

684 For two-photon imaging experiments, GCaMP6s expression in pyramidal neurons were generated
685 using the hybrid strain Camk2α-tTA;G6s2.

686 **General surgical procedures**

687 All surgeries were performed under 1-2% isoflurane in oxygen anesthesia. After induction of
688 anesthesia, 1.2 mg/kg of meloxicam was injected subcutaneously and sterile lidocaine ointment
689 was applied topically to the skin incision site. After making a midline cranial incision, the skin
690 was retracted laterally and fixed in position with tissue adhesive (Vetbond, 3M). We then built an
691 outer wall using dental cement (C&B Metabond, Parkell; Ortho-Jet, Lang Dental) along the lateral
692 edge of the dorsal cranium (frontal and parietal bones) to maximize the area of exposed skull. A
693 custom titanium skull post was then attached to the dental cement. For skull clearing, debris and
694 periosteum were thoroughly cleaned from the skull followed by the application of a thin layer of
695 cyanoacrylate (Zap-A-Gap CA+, Pacer technology).

696 To prepare mice for two-photon imaging, a circular craniotomy (ø = 3 mm) centered over the right
697 frontal cortex (1.75 mm lateral to midline and 1.75 mm rostral to bregma), was made using a
698 biopsy punch. A circular coverslip (ø = 3 mm) was then lowered to the surface of the brain and
699 Vetbond and Metabond were used to seal the window to the skull. Lastly, a titanium skull post
700 was implanted as described above.

701 **Viral injections**

702 After induction with isoflurane anesthesia, animals were placed in a stereotaxic frame (David Kopf
703 Instruments). The skull was leveled along the rostral-caudal and medio-lateral axis, allowing for
704 accurate and reproducible targeting. All injections were made using a programmable nanoliter
705 injector (Nanoject III, Drummond Scientific, PA). For *widefield imaging* of CStr mice, widespread
706 corticostriatal GCaMP6s expression was generated in Ai162;G6s2 reporter mice by performing
707 bilateral stereotaxic injections of CAV-2-Cre (at 3-4 weeks of age) into the dorsal striatum at three
708 targets per hemisphere spanning the rostro-caudal axis. The target coordinates (relative to bregma
709 and dura, in mm) are (1) RC +0.75, ML ±1.8, DV 3.0; (2) RC 0, ML ±2.2, DV 3.1; (3) RC -0.75,
710 ML ±2.9, DV 3.1. For each striatal target, a burr hole was created using a small dental burr
711 followed by injection of 1.8×109 purified particles (pp) of CAV-2-Cre using pipettes with long
712 taper tips pulled from borosilicate capillaries (3.5" Drummond # 3-000-203-G/X, Drummond
713 Scientific, PA). For *two-photon imaging* experiments, CStr neurons were labeled through striatal
714 injections of AAV-2-retro-CAG-tdTomato (using the same approach and coordinates as described
715 above) in Camk2α-tTA;G6s2 mice.

716 For cell type-specific *optogenetic silencing* experiments, we performed bilateral injections in
717 frontal, parietal, and auditory cortex (coordinates relative to bregma, in mm: frontal cortex: RC
718 +2.5, ML ±1.5; parietal cortices: RC -1.7, ML ±2.5; auditory cortex: RC -2.5, ML ±4.6) to
719 induce expression of Cre-dependent stGtACR2 (AAV1-hSyn-SIO-stGtACR2-FusionRed, Upenn
720 Vector Core, Supp. Table 2). Cortical injections were performed in P42 to P56 Fezf2-2A-CreER

721 (PT), PlexinD1-2A-CreER (IT), and EMX-Cre (nonspecific PyNs) reporter mice. In mice with
722 ligand-dependent Cre recombinase activity, intraperitoneal tamoxifen was administered one
723 week after viral injections. Injections were made at two depths (300 and 600 µm) per cortical
724 target. In two EMX-Cre mice, bilateral injections were performed in the frontal and visual cortex
725 (RC -4, ML ±2.5). To express stGtACR2 in CStr neurons, viral injections were performed in
726 C57BL/6J mice in two stages. In stage one, we utilized a viral receptor complementation
727 strategy[47] by injecting both AAV-DJ-hSYN-DIO-hCAR{off} and AAV1-SIO-hSyn1-
728 stGtACR2-FusionRed in different cortical locations (targets as described above) in P21-P28
729 mice. In stage two, we performed bilateral striatal CAV-2-Cre injections 6 weeks after the initial
730 cortical injections (see above). hCAR is expressed in all transfected neurons in a Cre-OFF
731 manner, meaning that Cre expression stops expression of hCAR while inducing expression of
732 stGtACR2.

733 **Optical fiber implantation**

734 For optogenetic silencing, we expressed the soma-targeted anion-conducting channelrhodopsin
735 stGtACR2 in target neuronal populations[46]. Optical fibers (NA = 0.36, ø = 0.4mm, FT400UMT,
736 Thorlabs) were glued into metal or ceramic ferrules (ø = 1.25 mm, Thorlabs) and secured above
737 the cortex following viral injections at each target. Ferrule-enclosed optical fiber implantations
738 immediately followed cortical AAV injections in Fezf2, PlexinD1, and Emx mice and striatal
739 CAV-2-Cre injections in CStr mice. One polished end of the optical fiber was positioned extradural
740 to the site of cortical injections and interfaced with thinned skull using cyanoacrylate. Next, the
741 fiber was fixed to the skull using light-cured glass ionomer (Vitrebond, 3M). Additional layers of
742 dental cement and dental acrylic (Lang Dental Jet Repair Acrylic; Part#1223MEH) were applied
743 around the fiber implant and the skull to reinforce for durability and long-term stability. After all
744 layers were cured, a final outer coating of cyanoacrylate and nail polish were applied.

745 **Behavioral training**

746 The behavioral setup was controlled with a microcontroller-based (Arduino Due) finite state
747 machine (Bpod r0.5, Sanworks) using custom Matlab code (2015b, Mathworks) running on a
748 Linux PC. Servo motors (Turnigy TGY-306G-HV) and touch sensors were controlled by
749 microcontrollers (Teensy 3.2, PJRC) running custom code. Fifty-four mice were trained on a
750 delayed, spatial discrimination task. Mice initiated trials by placing their forepaws on at least one
751 of the two handles, which were mounted on servo motors that rotated out of reach during the inter-
752 trial period. Upon trial initiation, animals placed their forepaws on the handles and, after a variable
753 duration of 0.25-0.75 seconds of continuous contact, the auditory stimulus was presented. Auditory
754 stimuli consisted of a sequence of Poisson-distributed, 3-ms long auditory click sounds[36],
755 presented from either a left and/or right speaker for a variable duration between 1 and 1.5 seconds.
756 The stimulus period was followed by a variable delay of up to 1 second, then the servo motors
757 moved two lick spouts into close proximity of the animal's mouth. If the animal licked twice on
758 the side where more clicks were presented, a drop of water reward was dispensed. The amount of
759 water rewarded per trial (typically 1.5 to 3 µl) was constant within a single session but was
760 sometimes adjusted daily based on the animal's body weight. After one spout has been licked
761 twice, the contralateral spout moved out of reach to force the animal to commit to its decision.

762 All trained mice were housed in groups of two or more under reverse light cycle (12- hour dark
763 and 12-hour light) and trained during their active dark cycle. Animals were trained over the course
764 of approximately 30-60 days. After 2-3 days of restricted water access, animals began habituation
765 to head fixation and received water from spouts in the behavior chamber. During these sessions,
766 unilateral auditory stimuli were presented followed by a droplet of water dispensed freely from the

767 ipsilateral water spout. After several habituation sessions, animals were then required to touch the
768 handles to trigger stimulus presentation. Once mice could reliably reach for the handles, the
769 required touch duration was progressively increased up to 0.75 seconds. During the next stage of
770 training, self-performed trials, where both spouts moved within reach of the animal following
771 stimulus presentation, were progressively introduced. An animal was considered trained when its
772 detection performance across two or more sessions was above 80%.

773 **Behavioral monitoring**

774 Data was collected from multiple sensors in the behavioral setup to measure different aspects of
775 animal movement. Touch sensors using a grounding circuit on handles and lick spouts detected
776 contact with the animal's forepaws and tongue, respectively. A piezo sensor (1740, Adafruit LLC)
777 below the animal's trunk was used for monitoring body and hindlimb movements. Two webcams
778 (C920 and B920, Logitech) were used for video recording of animal movements. Cameras were
779 positioned to capture the animal's face (side view) and the ventral surface of the body (ventral
780 view).

781 **Widefield imaging**

782 Widefield imaging was done as reported previously[23,32,81] using an inverted tandem-lens
783 macroscope in combination with an sCMOS camera (Edge 5.5, PCO) running at 30 fps. The top
784 lens had a focal length of 105 mm (DC-Nikkor, Nikon) and the bottom lens 85 mm (85M-S,
785 Rokinon). The field of view was 12.5 x 10.5 mm^2 and the imaging resolution was 640 x 540 pixels
786 after 4x spatial binning, resulting in a spatial resolution of ~20 µm per pixel. To capture GCaMP
787 fluorescence, a 525 nm band-pass filter (#86-963, Edmund optics) was placed in front of the
788 camera. Using excitation light at two different wavelengths, we isolated Ca^{2+}-dependent
789 fluorescence and corrected for intrinsic signals (e.g., hemodynamic responses)[22,25]. Excitation light
790 was projected on the cortical surface using a 495 nm long-pass dichroic mirror (T495lpxr, Chroma)
791 placed between the two macro lenses. The excitation light was generated by a collimated blue LED
792 (470 nm, M470L3, Thorlabs) and a collimated violet LED (405 nm, M405L3, Thorlabs) that were
793 coupled into the same excitation path using a dichroic mirror (#87-063, Edmund optics). We
794 alternated illumination between the two LEDs from frame to frame, resulting in one set of frames
795 with blue and the other with violet excitation at 15 fps each. Excitation of GCaMP at 405 nm
796 results in non-calcium dependent fluorescence[82], allowing us to isolate the true calcium-dependent
797 signal by rescaling and subtracting frames with violet illumination from the preceding frames with
798 blue illumination. All subsequent analysis was based on this differential signal. The imaging data
799 was then rigidly aligned to the Allen common coordinate framework (CCF), using four anatomical
800 landmarks: the left, center and right points where anterior cortex meets the olfactory bulbs, and
801 the medial point at the base of retrosplenial cortex. Retinotopic visual mapping experiments[31,83]
802 confirmed accurate CCF alignment and showed high correspondence between functionally
803 identified visual areas and the CCF across PyN types (Fig. 1c).

804 **Two-photon imaging**

805 We used a two-photon resonant scanning microscope (Moveable Objective Microscope, Sutter
806 Instruments) for session-long, continuous image acquisition at 30.9 Hz. A 16X, 0.8 NA Nikon
807 objective lens was used for single-plane imaging with a 512x512 pixels (575 µm x 575 µm) fields
808 of view. Mode-locked illumination at 930 nm was delivered using a Ti:Sapphire laser (Ultra II,
809 Coherent). Imaging frames were aligned with behavior control events synchronized acquisition of
810 analog galvanometric and Bpod output signals. Depth of focal planes was 200-400 µm below the
811 dura. Emission was collected using band-pass red (670/50 nm) and green (525/50 nm) filters

812 (Chroma Technologies). MScan software (Sutter Instruments) was used for image acquisition.
813 Recordings were performed in ALM (2.5 mm rostra and 1.5 mm lateral to bregma) or MM (1.5
814 mm anterior and 1 mm lateral to bregma) in randomized order across mice. Across imaging
815 session, we selected planes that differed from those of prior sessions in order to maximize the
816 number of unique neurons by.

817 Raw images were processed using the Suite2P package[84] which performed motion correction,
818 model-based ROI detection, correction for neuropil contamination, and spike deconvolution.
819 Somatic and non-somatic (neuropil) ROI identification was performed through a combination of
820 pre-trained classifier and manual curation. Somata with tdTomato expression were identified in a
821 two-step process. First, potential green channel bleed-through was subtracted from the red channel
822 using non-rigid regression with individual channels being divided into smaller blocks. Next, all
823 sessions were then manually inspected to identify a conservative red fluorescence threshold, which
824 was subsequently applied to all sessions. Analyses of neural activity were based on deconvolved
825 values ("inferred spiking activity"). Since the deconvolved values do not represent absolute firing
826 rates, we performed z-score normalization for each neuron before computing trial-averages across
827 cells. The total number of recorded neurons per session was 396 ± 105 (mean ± standard deviation).

828 **Optogenetic inactivation**

829 Photostimulation was performed using a 470 nm high-power LED (M470F3, Thorlabs) with a
830 power density of 25 mW/mm^2. Stimuli consisted of a square wave stimulus that ramped down in
831 power for 200 milliseconds, to avoid an excitatory post-illumination rebound due to sudden release
832 of inhibition[85]. To prevent animals' visual detection of photostimulation, either through external
833 leakage from light-insulated mating sleeves or transmission to the retina across the brain, an
834 external LED with matching wavelength placed at the center of the animal's visual field was
835 flashed throughout the duration of every trial. Photoinhibition was performed in 20% of total trials
836 and randomly interleaved between light-off trials. During each session, only bilateral frontal,
837 parietal or visual cortex inhibition was performed. Once an animal was habituated and able to
838 complete detection behavior trials with > 90% accuracy, optogenetic inactivation trials were
839 introduced. During these initial sessions, optogenetic inhibition was performed from the beginning
840 of the stimulus epoch until the end of the delay epoch. Additionally, we performed 0.5-second
841 inhibition during four pre-defined epochs of the detection behavior trials: (1) first half of the
842 stimulus, (2) second half of the stimulus, (3) delay, (4) response.

843 **Immunohistology, microscopy and image analysis**

844 For a given animal, after all experiments were concluded, we performed transcardial perfusion
845 with PBS followed by fixation with 4% PFA in 0.1 M PB. Brains were post-fixed in 4% PFA for
846 an additional 12-18 hours at 4°. Prior to sectioning, brains were rinsed three times in PBS and
847 embedded in 4% agarose-PBS. Slices 50 μm in thickness were made using a vibrating microtome
848 (Leica, VT100S). Sections were then suspended in blocking solution (10% Normal Goat Serum
849 and 0.1% Triton-X100 in 1X PBS) for 1 hour followed by overnight incubation at 4°C with the
850 primary antibody. Next, sections were washed with PBS, incubated for 1 h at room temperature
851 with the secondary antibody at 1:500 dilution. For visualization of GCaMP6s, we used primary
852 goat polyclonal anti-GFP antibody (Abcam) and secondary donkey anti-goat Alexa Fluor 488
853 (Abcam). Sections were then dry-mounted on slides using Vectashield (Vector Labs, H1000) prior
854 to imaging. No immunostaining was performed for the visualization of FusionRed or tdTomato.
855 Imaging was performed using upright fluorescence macroscope and microscope (Olympus BX61).
856 Images were acquired using Ocular Scientific Image Acquisition Software (Teledyne Imaging)
857 and visualization and analysis were performed using ImageJ/FIJI software packages.

858 **Quantification cortex-wide gene expression**

859 Quantification of cell counts across the dorsal cortex was performed using publicly available serial
860 two-photon tomography (STPT) datasets. (http://www.brainimagelibrary.org/)[26]. Cre expression
861 patterns for IT and PT neurons were characterized with data from eight mice, expressing either
862 Cre-dependent GFP (PlexinD1-2A-CreER;Snap25-LSL-2A-EGFP) or tdTomato (Fezf2-2A-
863 CreER;Ai14), respectively. Cell counting was then performed via automated soma detection, using
864 a trained convolutional neural network[86]. STPT datasets were then registered to the Allen CCF v3
865 using the elastix toolbox[87]. To obtain the density of Cre-expressing neurons for individual cortical
866 areas, we used the area outlines from the Allen CCF and computed the average sum of detected IT
867 or PT neuron in each area, normalized by its surface area.

868 **Preprocessing of neural data**

869 We first performed motion correction on each imaging frame, using a rigid-body image
870 registration method implemented in the frequency domain[88] that aligned each frame to the median
871 over all frames in the first trial. To reduce the computational cost of subsequent analyses, we then
872 computed the 200 highest-variance components using singular value decomposition (SVD). These
873 components accounted for at least 95% of the total variance in each recording, whereas computing
874 500 components accounted for little additional variance (~0.15%). SVD reduces the raw imaging
875 data Y to a matrix of 'spatial components' U (of size pixels by components), 'temporal
876 components' V^T (of size components by frames) and singular values S (of size components by
877 components) to scale temporal components to the original data. The resulting decomposition has
878 the form $Y = USV^T$. All subsequent analysis in the time domain (such as the encoder and decoder
879 models described below) were then performed on the product SV^T and the respective results were
880 later multiplied with U, to recover results for the original pixel space. To avoid slow drift in the
881 imaging data, SVT was high-pass filtered above 0.1 Hz using a zero-phase, second-order
882 Butterworth filter.

883 To compute trial averages and perform choice decoder analysis (see below), imaging data in
884 individual trials were aligned to the four trial periods, each marked by a specific event. This was
885 required because the duration of different trial events was randomized to reduce temporal
886 correlations, e.g. between trial initiation, the stimulus presentation and subsequent lick responses.
887 The first period (Initiate) was aligned to the time when animal initiated a trial by touching the
888 handles, the second (Stimulus) was aligned to the stimulus onset, the third (Delay) to the end of
889 the stimulus sequence, and the fourth (Response) to the time when spouts were moved in to allow
890 a lick response. After alignment, the total trial duration was 2 seconds and durations of respective
891 trial episodes were 0.5 (Initiate), 1 (Stimulus), 0.2 (Delay), and 0.3 seconds (Response).

892 **Spatial clustering and classification**

893 To obtain more interpretable spatial components and assess the dimensionality of cortical activity
894 in different PyN types, we used semi-nonnegative matrix factorization (sNMF). As with SVD,
895 sNMF also creates spatial and temporal components for each session and for each mouse but
896 enforces spatial components to be strictly positive. The reason why temporal components were not
897 also enforced to be non-negative is that our hemodynamic correction resulted in temporal
898 dynamics that can be either positive or negative, relative to baseline. We used the LocaNMF
899 toolbox by Saxena et al[33] (https://github.com/ikinsella/locaNMF) to transform the spatial and
900 temporal components U and SV^T into two corresponding matrices A and C, where A is a matrix
901 of non-negative spatial components (of size pixels by components) and C the corresponding
902 temporal components (of size components by frames). In addition to regular sNMF, the LocaNMF

903 toolbox can be initialized with spatial constraints that are based on the Allen CCF. To obtain
904 spatially restricted localized LocaNMF components, we constructed a map of larger seed regions
905 by merging several smaller areas in the Allen CCF together (Fig. 2e). This region map is then used
906 to enforce that each component in A is sparse outside the boundary of a given region. The amount
907 of possible overlap between regions is specified by a localization threshold which specifies the
908 percentage of a given component that is constrained to be inside a single region's boundary. To
909 obtain dense spatial components that were mostly driven by the local correlations between pixels
910 and could also lie at the border between seed regions, we used a localization threshold of 50%. To
911 obtain unconstrained sNMF spatial components, we also used the LocaNMF toolbox but only
912 provided a single region that spanned the entire cortex. This resulted in cortex-wide components,
913 similar to vanilla sNMF, while ensuring that all other analysis steps were done identically for
914 sNMF and LocaNMF components. In both cases, we determined how many components in A and
915 C were needed to explain 99% of the variance of Y (with Y=AC) after the initial SVD.

916 To compare spatial sNMF and LocaNMF components from different PyN types, we embedded
917 them in a 2-dimensional space, using Uniform Manifold Approximation and Projection (UMAP)
918 analysis (Fig. 2c,g). UMAP analysis was performed with the UMAP toolbox by McInnes et al.[35]
919 (https://github.com/lmcinnes/umap). For each recording, the first 20 spatial components in A
920 (either from sNMF or region-constrained LocaNMF) were downsampled by a factor of 2,
921 smoothed with a 2-D gaussian filter (5 x 5 pixels, 2 pixel standard deviation) and peak-normalized.
922 Components from all recordings and animals were then combined into a larger matrix (of size
923 pixels by components) and we used UMAP to project the first (pixel) dimension into two,
924 maximally separating non-linear dimensions. Each point in the two dimensional space (Fig. 2c,g)
925 therefore reflects a single component from one animal in a given imaging session.

926 The same UMAP approach was used for temporal sNMF and LocaNMF components. Before the
927 UMAP projection, we first computed the trial-averaged and z-scored activity of each component
928 to achieve temporal dynamics that are comparable across sessions and individual mice.

929 To identify PyN types based on individual spatial components (Fig. 2d, h), we performed a separate
930 UMAP projection for each mouse. Each of these projections excluded all components from the
931 test animal, ensuring that the UMAP projection was not shaped by potential noise patterns or other
932 unknown features of the test components that could affected the classifier result. We then tested
933 the first 20 components of each session of the test animal with 100 repetitions per component. In
934 every repetition, 1000 components from each PyN type were randomly selected from the pre-
935 computed UMAP space and we then assigned the PyN type of the test component based on the
936 identity of its 10 nearest neighbors in UMAP space. For LocaNMF components, we performed the
937 same procedure but additionally ensured to use an equal number of components from each seed
938 region and PyN type to prevent PyN types with a larger number of components in a given region
939 from biasing the classifier result. Classifier accuracy for each session (Fig. 2d,h) was then
940 computed as the mean probability over all repetitions to accurately identify the PyN type.

941 To determine the size of PyN-predictive LocaNMF components, we selected all spatial
942 components that achieved a classification accuracy of 99% percent or higher (all other components
943 were assigned as non-specific) and thresholded each component above 0.2 to obtain a binary
944 image. The size of each component was then computed as the square root of the sum of all pixels
945 and converted to square millimeters.

946 **Linear encoding model**

The linear encoding model was based on a combination of task- and movement-related variables, as described previously[32]. Each variable consisted of multiple regressors that were combined into a larger design matrix. Binary regressors contained a single pulse that signaled the occurrence of specific events, such as the stimulus onset, and additional regression copies that were shifted forward or backward in time to account for changes in cortical activity before or after the respective event. For auditory stimuli, the time-shifted copies spanned all frames from the onset of the auditory sequence until the end of the trial. Individual click sounds were also captured by an additional regressor set that spanned the 2 seconds after click onset. For motor events, like licking or whisking, the time-shifted copies spanned the frames from 1 s before until 2 s after each event. Lastly, for some variables, such as the previous choice, the time-shifted copies spanned the whole trial. Other variables were analog, such as measures from the piezo sensor or the pupil diameter, and also contained the 200 highest temporal components of video information from both cameras (using SVD as described above). This ensured that the model could account for animal movements and accurately isolate task-related activity. Movement and task variables were additionally decorrelated due to the variable durations of the initiation, stimulus and delay period. The model was fit using ridge regression to allow for similar contributions from different correlated variables. To determine the regularization penalty λ for each column of the widefield data, we used marginal maximum likelihood estimation (MLE)[89]. MLE expresses the encoding model as a Bayesian linear model and determines the ridge penalty λ by maximizing the marginal likelihood $\pi(D \mid \lambda)$ of the model, given data D. This was done iteratively by testing different λ values to determine a global minimum for the negative log-likelihood $-\log \pi(D \mid \lambda)$. The main advantage of this approach is that λ can be determined without computationally expensive cross-validation procedures, resulting in a ~50-fold decrease in required compute time on a regular work station. Moreover, the faster MLE approach allows adjusting λ values for individual widefield data components which results in higher cross-validated explained variance of the encoding model, compared to a regular cross-validation approach (Supp. Fig. 16).

Variance analysis

Explained variance (cvR^2) was obtained using 10-fold cross-validation. This was done by fitting the model weights to a continuous 90%-large section of the imaging data and then computing the explained variance in the remaining 10% of the data. The procedure was repeated for 10 times, while shifting the training and test data to ensure that each part of the recording was used in the test data in one of the folds. To assess unique explained variance by individual variables (ΔR^2), we created reduced models in which all regressors of a specific variable were shuffled in time. Shuffling of each regressor was done within individual trials to account for a potential impact of very slow temporal correlations due the kinetics of the calcium indicator. The difference in explained variance between the full and the reduced model yielded the unique contribution ΔR^2 of that model variable that could not be explained by other variables in the model. The same approach was used to compute unique contributions for groups of variables, i.e., 'Movements' and 'Task'. Here, all variables that corresponded to a given group were shuffled at once.

Decoding model

To predict animal's left/right choices from widefield data, we trained logistic regression decoders with an L1 penalty on the temporal component matrix SV^T in each session. The L1 penalty was defined as the inverse of the number of observations in the test dataset during cross-validation, which yielded a good balance between the cross-validated prediction accuracy of the decoder and the number of non-zero model regressors. When decoding choice, we randomly removed trials until there was an equal amount of correct and incorrect trials where mice chose the left and the right side. By balancing left/right choice sides and correct/incorrect trials, we ensured that the

decoder would not predict choices due to corresponding sensory information or would be influenced by potential side biases. The logistic regression model was implemented in Matlab using the 'fitclinear' function and run repeatedly for each time point in individual trials after re-aligning them to trial periods as described above. In each session, all decoder runs were performed with the same amount of trials (at least 250 trials) and we used 10-fold cross-validation to compute decoder accuracy at each time point in the trial. Beta weights were averaged from all models created during cross-validation and convolved with the spatial component matrix U to create cortical maps of the choice decoder weights.

Receiver operating characteristic (ROC) analysis

We computed the area under the ROC curve (AUC) to quantify choice preference of single neurons obtained from two-photon imaging. AUCs were computed by comparing the mean neural activity during the stimulus and delay period in all trials with ipsilateral versus contralateral choices. AUC values denote the specificity of the neural activity to ipsi- or contralateral choices, with values below 0.5 signifying ipsilateral choice-selectivity and AUC values above 0.5 contralateral choice-selectivity. To identify statistically significant choice-selective neurons, AUC values were also computed for shuffled trial labels (randomly assigning ipsi- and contralateral choices across trials) for each neuron. This procedure was repeated 100 times to create a distribution of shuffled AUC values for each neuron. A neuron's choice selectivity was then deemed significant if the probability of obtaining the actual AUC from the shuffled AUC distribution was less than 0.05.

Code availability statement: Code for preprocessing (e.g., hemodynamic correction and dimensionality reduction) is available here: https://github.com/churchlandlab/WidefieldImager/tree/master/Analysis. A cloud-based option for many of these steps is available at Neurocaas: http://neurocaas.org. To simplify the interaction with the online platform, a graphical user interface, dedicated to launching analysis and retrieving results from the NeuroCAAS platform is available here: (https://github.com/churchlandlab/wfield). Code for the ridge regression used in the encoding model is available on the lab's GitHub page: https://github.com/churchlandlab/ridgeModel.

Data availability statement: We will make preprocessed datasets from all animals available at time of publication. As in previous publications, we will also include a "readme" statement that explains how the data are stored. An example dataset has already been shared (DOI: 10.5281/zenodo.5834513) on Zenodo to demonstrate the feasibility of this pipeline: https://zenodo.org/record/5834513#.Yd3jHViZPX8.

1028 **Supplementary Table 1: Overview of different model variables**

1029

Variable name	Description	Variable type	Category
Hindlimb	Piezo sensor below the animal	Analog + Event kernel	Movement
Handles (Left / Right)	Touch events from handle sensors	Event kernel	Movement
Licks (Left / Right)	Lick events from spout sensors	Event kernel	Movement
Pupil	Pupil diameter, extracted from face camera	Analog + Event kernel	Movement
Nose	Nose movements, extracted from face camera	Analog + Event kernel	Movement
Whisking	Whisker movements, extracted from face camera	Analog + Event kernel	Movement
Body	Average motion energy across all body camera pixels	Analog + Event kernel	Movement
Video	Video dimensions from both cameras (SVD)	Analog	Movement
Video ME	Video dimensions from motion energy in both cameras	Analog	Movement
Choice (Left / Right)	All frames in either a left- or a rightward choice trial	Event kernel	Task
Previous choice	Every trial after a leftward choice trial	Event kernel	Task
Previous modality	Every trial after a visual trial	Event kernel	Task
Previous success	Every trial after a successful trial	Event kernel	Task
Success	All successful trials	Event kernel	Task
Water given	All frames after a water reward was given	Event kernel	Task
Auditory stimulus (Left / Right)	All frames after a left- or rightward auditory stimulus	Event kernel	Task
Visual stimulus (Left / Right)	All frames after a left- or rightward visual stimulus	Event kernel	Task

1030

1031 **Supplementary Table 2: Number of mice included for each experiment**

	Optogenetics	Widefield	Two-photon
Emx	9	4	-
CStr	9	4	-
Fezf2	8	5	-
PlexinD1	8	4	-
Camk2α-tTA;G6s2	-	-	3

1032

1033 **Supplementary Table 3: Resources**

Reagent/resource	Source	Identifier
Antibodies		
Goat polyclonal anti-GFP	Abcam	ab6673
Donkey Anti-Goat Alexa Fluor 488	Abcam	ab150129
Viral strains		
CAV-2-Cre	Plateforme de Vectorologie de Montpellier	N/A
AAV1-hSyn1-SIO-stGtACR2-FusionRed	Penn Vector Core	105677-AAV1
AAVrg-CAG-tdTomato	Penn Vector Core	59462-AAVrg
AAV-DJ-hSYN-DIO-hCAR{off} (Titer: 5.7e12 vg/ml)	Laboratory of Adam Kepecs	
Experimental Models		
Mouse: Emx1-IRES-Cre: Emx1$^{tm1(cre)Krj}$	The Jackson Laboratory	JAX#005628
Mouse: ROSA:LNL:tTA: Gt(ROSA)26Sor$^{tm1(tTA)Roos}$	The Jackson Laboratory	JAX#008600
Mouse: Camk2α-tTA: Tg(Camk2a-tTA)1Mmay	The Jackson Laboratory	JAX#003010
Mouse: Ai93(TITL-GCaMP6f)-D (Ai93D): Igs7$^{tm93.1(tetO-GCaMP6f)Hze}$	The Jackson Laboratory	JAX#024103
Mouse: Ai162(TIT2L-GC6s-ICL-tTA2)-D (Ai162D): Igs7$^{tm162.1(tetO-GCaMP6s,CAG-tTA2)Hze}$	H. Zeng, Allen Institute for Brain Science	JAX#031562
Mouse: TRE-GCaMP6s (G6s2): Tg(tetO-GCaMP6s)2Niell	The Jackson Laboratory	JAX#024742
Mouse: H2B-eGFP: Tg(HIST1H2BB/EGFP)1Pa	The Jackson Laboratory	JAX#006069
Mouse: Fezf2-2A-CreER: Fezf2$^{tm1.1(cre/ERT2)Zjh}$	The Jackson Laboratory	JAX#036296
Mouse: PlexinD1-2A-CreER: Plxnd1$^{tm2.1(flpo)Zjh}$	The Jackson Laboratory	JAX#036295
Software		
MATLAB 2018B	Mathworks	
Python 3.6.10	Python Software Foundation	
Other		
Bpod State Machine r0.5	Sanworks	N/A

1034

1035

References

1. Harris, K. D. & Mrsic-Flogel, T. D. Cortical connectivity and sensory coding. *Nature* **503**, 51–58 (2013).
2. Pfeffer, C. K., Xue, M., He, M., Huang, Z. J. & Scanziani, M. Inhibition of Inhibition in Visual Cortex: The Logic of Connections Between Molecularly Distinct Interneurons. *Nat Neurosci* **16**, 1068–1076 (2013).
3. Keller, A. J. *et al.* A Disinhibitory Circuit for Contextual Modulation in Primary Visual Cortex. *Neuron* **108**, 1181-1193.e8 (2020).
4. Tremblay, R., Lee, S. & Rudy, B. GABAergic Interneurons in the Neocortex: From Cellular Properties to Circuits. *Neuron* **91**, 260–292 (2016).
5. Cardin, J. A. *et al.* Driving fast-spiking cells induces gamma rhythm and controls sensory responses. *Nature* **459**, 663–667 (2009).
6. Veit, J., Hakim, R., Jadi, M. P., Sejnowski, T. J. & Adesnik, H. Cortical gamma band synchronization through somatostatin interneurons. *Nature Neuroscience* **20**, 951–959 (2017).
7. Sohal, V. S., Zhang, F., Yizhar, O. & Deisseroth, K. Parvalbumin neurons and gamma rhythms enhance cortical circuit performance. *Nature* **459**, 698–702 (2009).
8. Reimer, J. *et al.* Pupil fluctuations track fast switching of cortical states during quiet wakefulness. *Neuron* **84**, 355–362 (2014).
9. Fu, Y. *et al.* A Cortical Circuit for Gain Control by Behavioral State. *Cell* **156**, 1139–1152 (2014).
10. Zhou, M. *et al.* Scaling down of balanced excitation and inhibition by active behavioral states in auditory cortex. *Nature Neuroscience* **17**, 841–850 (2014).
11. Polack, P.-O., Friedman, J. & Golshani, P. Cellular mechanisms of brain state–dependent gain modulation in visual cortex. *Nature Neuroscience* **16**, 1331–1339 (2013).
12. Tasic, B. *et al.* Shared and distinct transcriptomic cell types across neocortical areas. *Nature* **563**, 72–78 (2018).
13. Economo, M. N. *et al.* Distinct descending motor cortex pathways and their roles in movement. *Nature* **563**, 79–84 (2018).
14. Chen, J. L., Carta, S., Soldado-Magraner, J., Schneider, B. L. & Helmchen, F. Behaviour-dependent recruitment of long-range projection neurons in somatosensory cortex. *Nature* **499**, 336–340 (2013).
15. Glickfeld, L. L., Andermann, M. L., Bonin, V. & Reid, R. C. Cortico-cortical projections in mouse visual cortex are functionally target specific. *Nat Neurosci* **16**, 219–226 (2013).
16. Kim, T. *et al.* Cortically projecting basal forebrain parvalbumin neurons regulate cortical gamma band oscillations. *PNAS* **112**, 3535–3540 (2015).
17. Harris, K. D. & Shepherd, G. M. G. The neocortical circuit: themes and variations. *Nature Neuroscience* **18**, 170–181 (2015).
18. Takahashi, N. *et al.* Active dendritic currents gate descending cortical outputs in perception. *Nature Neuroscience* 1–9 (2020) doi:10.1038/s41593-020-0677-8.
19. Tang, L. & Higley, M. J. Layer 5 Circuits in V1 Differentially Control Visuomotor Behavior. *Neuron* **105**, 346-354.e5 (2020).
20. Li, N., Chen, T.-W., Guo, Z. V., Gerfen, C. R. & Svoboda, K. A motor cortex circuit for motor planning and movement. *Nature* **519**, 51–56 (2015).
21. Chen, T.-W., Li, N., Daie, K. & Svoboda, K. A Map of Anticipatory Activity in Mouse Motor Cortex. *Neuron* **94**, 866-879.e4 (2017).
22. Wekselblatt, J. B., Flister, E. D., Piscopo, D. M. & Niell, C. M. Large-scale imaging of cortical dynamics during sensory perception and behavior. *Journal of Neurophysiology* **115**, 2852–2866 (2016).

23. Couto, J. *et al.* Chronic, cortex-wide imaging of specific cell populations during behavior. *Nat Protoc* 1–25 (2021) doi:10.1038/s41596-021-00527-z.
24. Cardin, J. A., Crair, M. C. & Higley, M. J. Mesoscopic Imaging: Shining a Wide Light on Large-Scale Neural Dynamics. *Neuron* **108**, 33–43 (2020).
25. Allen, W. E. *et al.* Global Representations of Goal-Directed Behavior in Distinct Cell Types of Mouse Neocortex. *Neuron* **94**, 891-907.e6 (2017).
26. Matho, K. S. *et al.* Genetic dissection of the glutamatergic neuron system in cerebral cortex. *Nature* **598**, 182–187 (2021).
27. Gerfen, C. R., Paletzki, R. & Heintz, N. GENSAT BAC cre-recombinase driver lines to study the functional organization of cerebral cortical and basal ganglia circuits. *Neuron* **80**, 1368–1383 (2013).
28. Harris, J. A. *et al.* Anatomical characterization of Cre driver mice for neural circuit mapping and manipulation. *Front Neural Circuits* **8**, 76 (2014).
29. Daigle, T. L. *et al.* A Suite of Transgenic Driver and Reporter Mouse Lines with Enhanced Brain-Cell-Type Targeting and Functionality. *Cell* **174**, 465-480.e22 (2018).
30. Wang, Q. *et al.* The Allen Mouse Brain Common Coordinate Framework: A 3D Reference Atlas. *Cell* **181**, 936-953.e20 (2020).
31. Garrett, M. E., Nauhaus, I., Marshel, J. H. & Callaway, E. M. Topography and Areal Organization of Mouse Visual Cortex. *J. Neurosci.* **34**, 12587–12600 (2014).
32. Musall, S., Kaufman, M. T., Juavinett, A. L., Gluf, S. & Churchland, A. K. Single-trial neural dynamics are dominated by richly varied movements. *Nat Neurosci* **22**, 1677–1686 (2019).
33. Saxena, S. *et al.* Localized semi-nonnegative matrix factorization (LocaNMF) of widefield calcium imaging data. *PLOS Computational Biology* **16**, e1007791 (2020).
34. Condylis, C. *et al.* Dense functional and molecular readout of a circuit hub in sensory cortex. *Science* **375**, eabl5981 (2022).
35. McInnes, L., Healy, J. & Melville, J. UMAP: Uniform Manifold Approximation and Projection for Dimension Reduction. *arXiv:1802.03426 [cs, stat]* (2018).
36. Brunton, B. W., Botvinick, M. M. & Brody, C. D. Rats and Humans Can Optimally Accumulate Evidence for Decision-Making. *Science* **340**, 95–98 (2013).
37. Salkoff, D. B., Zagha, E., McCarthy, E. & McCormick, D. A. Movement and Performance Explain Widespread Cortical Activity in a Visual Detection Task. *Cereb Cortex* **30**, 421–437 (2020).
38. Orsolic, I., Rio, M., Mrsic-Flogel, T. D. & Znamenskiy, P. Mesoscale cortical dynamics reflect the interaction of sensory evidence and temporal expectation during perceptual decision-making. *Neuron* **109**, 1861-1875.e10 (2021).
39. Steinmetz, N. A., Zatka-Haas, P., Carandini, M. & Harris, K. D. Distributed coding of choice, action and engagement across the mouse brain. *Nature* **576**, 266–273 (2019).
40. Bergmann, R. *et al.* Predicting behavior from eye movement and whisking asymmetry. 2021.02.11.430785 Preprint at https://doi.org/10.1101/2021.02.11.430785 (2021).
41. Esmaeili, V. *et al.* Rapid suppression and sustained activation of distinct cortical regions for a delayed sensory-triggered motor response. *Neuron* **109**, 2183-2201.e9 (2021).
42. Hanks, T. D. *et al.* Distinct relationships of parietal and prefrontal cortices to evidence accumulation. *Nature* **520**, 220–223 (2015).
43. Goard, M. J., Pho, G. N., Woodson, J. & Sur, M. Distinct roles of visual, parietal, and frontal motor cortices in memory-guided sensorimotor decisions. *eLife* **5**, e13764 (2016).
44. Peters, A. J., Fabre, J. M. J., Steinmetz, N. A., Harris, K. D. & Carandini, M. Striatal activity topographically reflects cortical activity. *Nature* 1–6 (2021) doi:10.1038/s41586-020-03166-8.
45. Oh, S. W. *et al.* A mesoscale connectome of the mouse brain. *Nature* **508**, 207–214 (2014).

46. Mahn, M. *et al.* High-efficiency optogenetic silencing with soma-targeted anion-conducting channelrhodopsins. *Nature Communications* **9**, 4125 (2018).
47. Li, S.-J., Vaughan, A., Sturgill, J. F. & Kepecs, A. A Viral Receptor Complementation Strategy to Overcome CAV-2 Tropism for Efficient Retrograde Targeting of Neurons. *Neuron* **98**, 905-917.e5 (2018).
48. Znamenskiy, P. & Zador, A. M. Corticostriatal neurones in auditory cortex drive decisions during auditory discrimination. *Nature* **497**, 482–485 (2013).
49. Guo, Z. V. *et al.* Flow of Cortical Activity Underlying a Tactile Decision in Mice. *Neuron* **81**, 179–194 (2014).
50. MacDowell, C. J. & Buschman, T. J. Low-Dimensional Spatiotemporal Dynamics Underlie Cortex-wide Neural Activity. *Current Biology* **30**, 2665-2680.e8 (2020).
51. Stringer, C. *et al.* Spontaneous behaviors drive multidimensional, brainwide activity. *Science* **364**, eaav7893 (2019).
52. Logothetis, N. K. *et al.* Hippocampal-cortical interaction during periods of subcortical silence. *Nature* **491**, 547–553 (2012).
53. Rogers, B. P., Morgan, V. L., Newton, A. T. & Gore, J. C. Assessing Functional Connectivity in the Human Brain by FMRI. *Magn Reson Imaging* **25**, 1347–1357 (2007).
54. Vanni, M. P. & Murphy, T. H. Mesoscale Transcranial Spontaneous Activity Mapping in GCaMP3 Transgenic Mice Reveals Extensive Reciprocal Connections between Areas of Somatomotor Cortex. *J. Neurosci.* **34**, 15931–15946 (2014).
55. Vanni, M. P., Chan, A. W., Balbi, M., Silasi, G. & Murphy, T. H. Mesoscale Mapping of Mouse Cortex Reveals Frequency-Dependent Cycling between Distinct Macroscale Functional Modules. *J. Neurosci.* **37**, 7513–7533 (2017).
56. Macé, É. *et al.* Whole-Brain Functional Ultrasound Imaging Reveals Brain Modules for Visuomotor Integration. *Neuron* **100**, 1241-1251.e7 (2018).
57. Matsui, T., Murakami, T. & Ohki, K. Transient neuronal coactivations embedded in globally propagating waves underlie resting-state functional connectivity. *PNAS* **113**, 6556–6561 (2016).
58. Huang, L. *et al.* BRICseq Bridges Brain-wide Interregional Connectivity to Neural Activity and Gene Expression in Single Animals. *Cell* **182**, 177-188.e27 (2020).
59. Mohajerani, M. H. *et al.* Spontaneous cortical activity alternates between motifs defined by regional axonal projections. *Nat Neurosci* **16**, 1426–1435 (2013).
60. Lohani, S. *et al. Dual color mesoscopic imaging reveals spatiotemporally heterogeneous coordination of cholinergic and neocortical activity*. 2020.12.09.418632 https://www.biorxiv.org/content/10.1101/2020.12.09.418632v1 (2020) doi:10.1101/2020.12.09.418632.
61. Gilad, A. & Helmchen, F. Spatiotemporal refinement of signal flow through association cortex during learning. *Nature Communications* **11**, 1–14 (2020).
62. Gallero-Salas, Y. *et al.* Sensory and Behavioral Components of Neocortical Signal Flow in Discrimination Tasks with Short-Term Memory. *Neuron* **109**, 135-148.e6 (2021).
63. Park, J. M. *et al.* Deep and superficial layers of the primary somatosensory cortex are critical for whisker-based texture discrimination in mice. *bioRxiv* 2020.08.12.245381 (2020) doi:10.1101/2020.08.12.245381.
64. Gilad, A., Gallero-Salas, Y., Groos, D. & Helmchen, F. Behavioral Strategy Determines Frontal or Posterior Location of Short-Term Memory in Neocortex. *Neuron* **99**, 814-828.e7 (2018).
65. Jun, E. J. *et al.* Causal role for the primate superior colliculus in the computation of evidence for perceptual decisions. *Nat Neurosci* (2021) doi:10.1038/s41593-021-00878-6.

66. Wang, L., McAlonan, K., Goldstein, S., Gerfen, C. R. & Krauzlis, R. J. A Causal Role for Mouse Superior Colliculus in Visual Perceptual Decision-Making. *J. Neurosci.* **40**, 3768–3782 (2020).
67. Felsen, G. & Mainen, Z. F. Neural substrates of sensory-guided locomotor decisions in the rat superior colliculus. *Neuron* **60**, 137–148 (2008).
68. Duan, C. A. *et al.* A cortico-collicular pathway for motor planning in a memory-dependent perceptual decision task. *Nature Communications* **12**, 2727 (2021).
69. Erlich, J. C., Brunton, B. W., Duan, C. A., Hanks, T. D. & Brody, C. D. Distinct effects of prefrontal and parietal cortex inactivations on an accumulation of evidence task in the rat. *eLife Sciences* **4**, e05457 (2015).
70. Raposo, D., Kaufman, M. T. & Churchland, A. K. A category-free neural population supports evolving demands during decision-making. *Nat Neurosci* **17**, 1784–1792 (2014).
71. Harvey, C. D., Coen, P. & Tank, D. W. Choice-specific sequences in parietal cortex during a virtual-navigation decision task. *Nature* **484**, 62–68 (2012).
72. Pinto, L. *et al.* Task-Dependent Changes in the Large-Scale Dynamics and Necessity of Cortical Regions. *Neuron* **104**, 810-824.e9 (2019).
73. Licata, A. M. *et al.* Posterior Parietal Cortex Guides Visual Decisions in Rats. *J. Neurosci.* **37**, 4954–4966 (2017).
74. Zatka-Haas, P., Steinmetz, N. A., Carandini, M. & Harris, K. D. Sensory coding and the causal impact of mouse cortex in a visual decision. *eLife* **10**, e63163 (2021).
75. Kim, J.-H., Ma, D.-H., Jung, E., Choi, I. & Lee, S.-H. Gated feedforward inhibition in the frontal cortex releases goal-directed action. *Nat Neurosci* **24**, 1452–1464 (2021).
76. Wu, Z. *et al.* Context-Dependent Decision Making in a Premotor Circuit. *Neuron* **106**, 316-328.e6 (2020).
77. Coen, P., Sit, T. P. H., Wells, M. J., Carandini, M. & Harris, K. D. *Mouse frontal cortex mediates additive multisensory decisions*. 2021.04.26.441250 https://www.biorxiv.org/content/10.1101/2021.04.26.441250v2 (2021) doi:10.1101/2021.04.26.441250.
78. Park, J., Phillips, J. W., Martin, K. A., Hantman, A. W. & Dudman, J. T. *Descending neocortical output critical for skilled forelimb movements is distributed across projection cell classes*. 772517 https://www.biorxiv.org/content/10.1101/772517v3 (2021) doi:10.1101/772517.
79. Callaway, E. M. *et al.* A multimodal cell census and atlas of the mammalian primary motor cortex. *Nature* **598**, 86–102 (2021).
80. Laboulaye, M. A., Duan, X., Qiao, M., Whitney, I. E. & Sanes, J. R. Mapping Transgene Insertion Sites Reveals Complex Interactions Between Mouse Transgenes and Neighboring Endogenous Genes. *Frontiers in Molecular Neuroscience* **11**, 385 (2018).
81. Ratzlaff, E. H. & Grinvald, A. A tandem-lens epifluorescence macroscope: hundred-fold brightness advantage for wide-field imaging. *J. Neurosci. Methods* **36**, 127–137 (1991).
82. Lerner, T. N. *et al.* Intact-Brain Analyses Reveal Distinct Information Carried by SNc Dopamine Subcircuits. *Cell* **162**, 635–647 (2015).
83. Marshel, J. H., Garrett, M. E., Nauhaus, I. & Callaway, E. M. Functional Specialization of Seven Mouse Visual Cortical Areas. *Neuron* **72**, 1040–1054 (2011).
84. Pachitariu, M. *et al.* Suite2p: beyond 10,000 neurons with standard two-photon microscopy. *bioRxiv* 061507 (2016) doi:10.1101/061507.
85. Chuong, A. S. *et al.* Noninvasive optical inhibition with a red-shifted microbial rhodopsin. *Nat Neurosci* **17**, 1123–1129 (2014).
86. Kim, Y. *et al.* Brain-wide Maps Reveal Stereotyped Cell-Type-Based Cortical Architecture and Subcortical Sexual Dimorphism. *Cell* **171**, 456-469.e22 (2017).

87. Klein, S., Staring, M., Murphy, K., Viergever, M. A. & Pluim, J. P. W. elastix: A Toolbox for Intensity-Based Medical Image Registration. *IEEE Transactions on Medical Imaging* **29**, 196–205 (2010).
88. Reddy, B. S. & Chatterji, B. N. An FFT-based technique for translation, rotation, and scale-invariant image registration. *IEEE Trans Image Process* **5**, 1266–1271 (1996).
89. Karabatsos, G. Marginal maximum likelihood estimation methods for the tuning parameters of ridge, power ridge, and generalized ridge regression. *Communications in Statistics - Simulation and Computation* (2017).